Accepted Manuscript

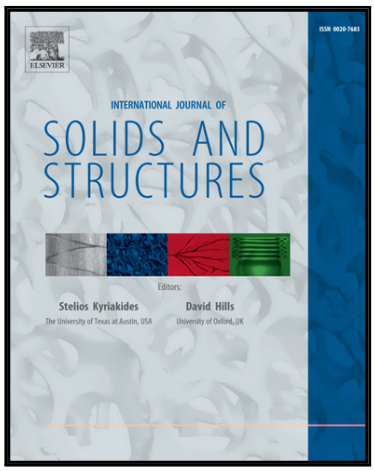

Numerical modeling of time- and temperature-dependent strain-induced crystallization in rubber

R. Behnke, T. Berger, M. Kaliske

PII: S0020-7683(18)30045-3
DOI: 10.1016/j.ijsolstr.2018.01.034
Reference: SAS 9883

To appear in: *International Journal of Solids and Structures*

Received date: 25 September 2017
Revised date: 24 January 2018
Accepted date: 26 January 2018

Please cite this article as: R. Behnke, T. Berger, M. Kaliske, Numerical modeling of time- and temperature-dependent strain-induced crystallization in rubber, *International Journal of Solids and Structures* (2018), doi: 10.1016/j.ijsolstr.2018.01.034

This is a PDF file of an unedited manuscript that has been accepted for publication. As a service to our customers we are providing this early version of the manuscript. The manuscript will undergo copyediting, typesetting, and review of the resulting proof before it is published in its final form. Please note that during the production process errors may be discovered which could affect the content, and all legal disclaimers that apply to the journal pertain.

ACCEPTED MANUSCRIPT

Highlights

- Temperature]dependent SIC is modeled at the microscale via an FE representation.
- Modeling of time]dependent SIC kinetics is addressed.
- SIC is computed for the principal directions of the strain field.
- Induced anisotropy effects in the material's mechanical and thermal response are captured.
- SIC on the microscale is computed from the structural response of a steady state rolling tire.

ACCEPTED MANUSCRIPT

ACCEPTED MANUSCRIPT

Numerical modeling of time- and temperature-dependent strain-induced crystallization in rubber

R. Behnke[a], T. Berger[a], M. Kaliske[a,*]

[a]*Institut für Statik und Dynamik der Tragwerke (ISD), Technische Universität Dresden, Fakultät Bauingenieurwesen, 01062 Dresden, Germany, Tel.: +49-351-46334386, Fax: +49-351-46337086*

Abstract

Besides the numerical representation of elastic properties of elastomers, a thermo-mechanical finite element model to capture strain-induced crystallization (SIC) in elastomers under static and dynamic loading is proposed in this contribution. The reinforcement effect resulting from SIC is assumed to be strain-, time- and temperature-dependent and is modeled on the microscale. Due to the orientation of crystallized domains along the principal stretch directions, anisotropy in the material's mechanical and thermal response is captured by the proposed model. Model parameters for the SIC process and its kinetics are identified based on previously published wide-angle X-ray diffraction (WAXD) results. Numerical studies and comparisons to experimental data reveal the features of the numerical model for SIC. Within a structural example, the material model for strain-crystallizable elastomers is employed to reveal SIC in steady state rolling tires modeled within the finite element framework via a micro-meso-macro transition of the deformation and temperature field involved.

Keywords: Strain-induced crystallization, elastomers, time dependency, temperature dependency, thermo-mechanical coupling, finite element method

ACCEPTED MANUSCRIPT

ACCEPTED MANUSCRIPT

1. Introduction

Strain-induced crystallization (SIC) is a specific process observed in a certain group of polymers (elastomers) subjected to significant large deformations [1]. A priori, SIC takes place at the molecular scale. However, the consequences of SIC significantly affect the macroscopic material response. The reinforcing mechanisms of SIC on the micro- and mesoscale contribute to the substantial improvement of the crack growth resistance of natural rubber (NR) [2] from which standard engineering applications involving elastomer products (tires, components, bearings etc.) could take advantage. As a first approximation, crystallites can be interpreted as additional crosslinking points or as rigid reinforcing particles strengthening the initially amorphous rubber [3, 4]. SIC leads to an increase of the strength at rupture, the large strain modulus and the crack propagation behavior of NR compared to the properties of non-crystallizing synthetic rubbers [5, 6, 7]. The strain-induced process leads to a rearrangement of the molecular structure from its ground amorphous state to a higher ordered (regular) state. The energy required for this process mainly stems from the externally applied loading (external work) yielding a measurable reinforcement mechanism (strengthening) of the material. During unloading, SIC is reversible in terms of the melting of crystallized domains. However, as observed in many experimental investigations, the specific strain-, time- and temperature-dependent kinetics of SIC result in the formation of additional hystereses (loading and unloading path) of a specimen under cyclic loading. Since the SIC process is triggered by the maximum strain field direction, the amorphous phase and the crystallized phase of the elastomer generate in total an anisotropic mechanical and thermal material

*Corresponding author
Email address: michael.kaliske@tu-dresden.de (M. Kaliske)

ACCEPTED MANUSCRIPT

behavior [8]. NR also undergoes thermally induced crystallization (TIC) at low temperatures [9, 10]. The developing crystal structure is the same but the crystal morphology is different.

The current explanation for SIC is that highly stretched, oriented segments between crosslinks undergo coil-to-stretch transformations forming extended chain crystals [11, 12]. In [13], the time dependency of SIC in crosslinked NR is experimentally studied by using synchrotron wide-angle X-ray diffraction (WAXD). Due to a time resolution in the millisecond range, time-dependent SIC during dynamic loading could be observed in dynamic mechanical tests and tensile impact tests. It is found that the dynamic loading significantly influences the degree of crystallinity compared to an equilibrium strain state (statics) showing SIC. Due to the time dependency observed, the degree of crystallinity is lower for dynamic loading [14], which leads to an additional contribution to the frequency dependency of the mechanical properties of elastomers.

Since the reinforcing mechanisms of SIC are of interest in order to outperform other materials with lower resistance to mechanical loading, SIC attracted various scientists over the last decades [15]. Besides experimental characterizations, numerical investigations and models gained interest from many researchers in order to explain the experimental observations and, in turn, to stimulate new experimental methods and phenomena to be investigated. The classic thermodynamic theory on SIC in NR [16] states that stretching of a rubber chain reduces its number of possible conformations and, in consequence, its entropy. This consideration of a thermodynamic equilibrium neglects any effects of SIC kinetics. In [17], the crystallization process is modeled in a more advanced form. While the stress-strain behavior of the amorphous phase is derived from entropy elasticity, the crystalline phase does not contribute to the strain energy (assump-

ACCEPTED MANUSCRIPT

tion of a nearly rigid crystalline phase with negligible entropy). The model allows to represent an anisotropic crystal morphology. A model to capture the thermo-mechanical response of NR during and after crystallization is proposed in [18, 19, 20]. First, the general theory to model thermo-mechanical effects of crystallization in NR is presented in [18]. Second, thermodynamic properties (heat capacity, melting temperature etc.) are addressed in [19]. Third, model parameters are identified based on existing mechanical test results in [20]. It has to be mentioned that the model concentrates on the representation of equilibrium states of SIC, it does not capture any strain-rate dependency. A model that accounts for the invariance of SIC with respect to the crosslink density is proposed in [4]. The model assumes a fluid-like phase, which remains unorientated under strain and which does not participate in the SIC process, whereas the rubber-like phase of the material exhibits rubber elasticity and contributes to SIC. In [21, 22], a phase field model based on the Flory theory of entropy-elasticity is introduced in order to numerically represent the crystal phase growing in an amorphous matrix of, e.g. a crystallizable elastomer. Several WAXD studies show the isotropy of a large material fraction [23, 24]. However, this description of the directional properties of the strain-crystallized material may be too simple [3]. Recently proposed models for SIC [25] take also into account anisotropic effects by introducing the crystallinity as an internal variable within a 1D model. Commonly, the micro-sphere approach is then used for the transition from the 1D model to the fully 3D model [26] with anisotropic features due to the independent evolution of the crystallinity in each direction of the micro-sphere or to incorporated time-dependent effects of SIC kinetics as addressed in [27]. In [28], thermo-elasticity and SIC are addressed by using the concept of the representative directions. Recently, the non-affine micro-sphere approach is also used in [29] to

ACCEPTED MANUSCRIPT

derive a micro-mechanically based continuum model at the microscale (free energy function) assuming that SIC reduces the entropy of semi-crystalline chains. Furthermore, an affine full network model for SIC based on these non-Gaussian chain statistics for a single crystallizing polymer chain has been proposed in [30] considering a rate-independent evolution law for the degree of crystallinity in an isothermal setting.

In [31], it is pointed out that especially the kinetics of SIC play an important role to correctly characterize the short-term behavior of NR within a rolling tire. Thermal effects of SIC processes can be studied by thermography, but separation of heating effects related to SIC and dissipative material features is hard to accomplish in experiments. For carbon black filled NR samples, investigations with respect to SIC have been carried out in [31] to also account for dissipative heating and convective cooling during testing. Therefore, a combination of deformation experiments with simultaneous synchrotron X-ray scattering as well as thermography is proposed in [31] to simultaneously separate the crystallization-dependent heat production or adsorption form dissipative processes in the rubber material and to track the time dependency of the processes taking place. In the same direction, a broader experimental scale (characterization of SIC by additional on-line measurements of the surface temperature by an infrared camera) has been recently proposed in [32], where an approach to separate the temperature contributions stemming from dissipative material, crystallization and energy loss to the surroundings is discussed.

Although SIC is an outstanding feature of a certain group of elastomers, its significance for engineering applications is limited a priori. On the one hand, SIC only takes place at significant large strains/deformations. On the other hand, the strain range of typical engineering applications lies in the small strain regime

ACCEPTED MANUSCRIPT

and does not exceed certain limit values to guarantee the product's service state. Although only moderate strains are present on the macroscale, on the meso- and microscale, large strains may occur due to sliding of contacting surfaces, local defects, material inhomogeneities or dislocations, e.g. in the vicinity of a crack tip. The latter case shall be exemplarily studied in more detail in this contribution. In consequence, SIC appears in scenarios in which typical strain limits are exceeded. The finite element method (FEM) is a widely used numerical method in engineering. Therefore, a certain interest is present to also incorporate the phenomena of SIC into advanced finite element (FE) material models. First, the idea is to render the existing material models more realistic. Second, the positive reinforcing effects of SIC can also be included on the structural scale to better understand the structural response of the polymer components under investigation [1].

Outline The outline is as following: In Section 2, a numerical material model for time- and temperature-dependent SIC is presented, which is based on the microscale. The model represents the amorphous elastomer phase (matrix) and the semi-crystalline phase (unidirectional reinforcement in principal strain directions) on the microscale. In contrast to other micromechanically based models for SIC, the present model makes use of an FE discretization of both phases, assembled in the form of a unit cube. The amorphous phase represents the thermoelastic properties of an uncrystallized elastomer in its ground state. For the reinforcing SIC processes, a strain-, temperature- and time-dependent unidirectional reinforcing element evolves in each of the three principal strain field directions according to the associated microscopical strain and temperature field as a function of time. In Section 3, the features of the proposed microscale model are demonstrated for tensile experiments and the time dependency of SIC kinetics is

ACCEPTED MANUSCRIPT

addressed. Finally in Section 4, the material model is employed in the framework of the FEM to compute SIC effects for a steady state rolling tire. The intention of this present study is to close the gap between the modeling of SIC at a local point on the one hand and its structural incorporation for engineering applications on the other hand.

2. Material model including strain-induced reinforcement

In this section, the material model representing the material behavior at the microscale is presented. The model approach consists of two phases (amorphous and semi-crystalline), which coexist in parallel to each other. First the amorphous rubber phase is discussed. Second, the semi-crystalline reinforcing phase is introduced.

2.1. Continuum mechanical setting

On the macroscale, a homogeneous body $\mathfrak{B} \subset \mathbb{R}^3$ consisting of material particles with position vector $\mathbf{X} \in \mathfrak{B}$ of the reference configuration at time $t = 0$ is considered and forms a continuum. At time $t > 0$, the material particles are located at the position $\mathbf{x}$ of the deformed body $\mathfrak{b} \subset \mathbb{R}^3$. The deformation map $\boldsymbol{\varphi}(\mathbf{X}, t) : \mathfrak{B} \times \mathbb{R}^3 \rightarrow \mathbb{R}^3$ with the property $\mathbf{x} = \boldsymbol{\varphi}(\mathbf{X}, t)$ and $\mathfrak{b} = \boldsymbol{\varphi}(\mathfrak{B}, t)$ relates the reference and the current configuration. The relative displacement of a material particle $\mathbf{u}$ at time $t \geq 0$ is computed from its initial and current position, i.e. $\mathbf{u} = \mathbf{x} - \mathbf{X}$. On the macroscale, the deformation gradient of the homogeneous body is introduced as

$$\mathbf{F} = \nabla_{\mathbf{X}} \boldsymbol{\varphi}(\mathbf{X}, t)\,, \tag{1}$$

representing the gradient of the mapping. The symbols $\nabla_{\mathbf{X}}\square$ and $\nabla_{\mathbf{x}}\square$ are used to denote the gradient operator with respect to the reference configuration and

ACCEPTED MANUSCRIPT

the current configuration, respectively. Furthermore, the absolute temperature $\Theta > 0$ of a material particle will be used in the following.

The deformation field of the microscale is governed by the deformation state of the macroscopic point $\mathbf{x}$ considered and, therefore, is a function of the macroscopic deformation gradient $\mathbf{F}$. For the representative volume element (RVE) of the microscale, a unit cube is considered as illustrated in Fig. 1. The deformation state of the unit cube is uniquely defined if the Cartesian axis system of the unit cube coincides with the axis system of the principal stretch directions $\mathbf{n}_1$, $\mathbf{n}_2$ and $\mathbf{n}_3$ of the deformation field of the macroscale. The temperature distribution of the microscale is considered as homogeneous (uniform temperature state).

The free energy function of the two-phase material is given as the sum of the contributions stemming from the amorphous phase and the semi-crystalline phase,

$$\Psi = \Psi_{\text{am}} + \Psi_{\text{cry}} \,. \tag{2}$$

In the following, the function type of the different contributions Ψ_{am} and Ψ_{cry} is discussed in more detail.

2.2. Amorphous phase

A different treatment of volume-preserving deformations and deformations with volume change are represented within the model by a multiplicative decomposition of the deformation gradient at the mircoscale in the form of

$$\mathbf{F} = \bar{\mathbf{F}}\,\mathbf{F}_{\text{vol}} \,, \quad \mathbf{F}_{\text{vol}} = J^{\frac{1}{3}}\mathbf{1}, \quad \bar{\mathbf{F}} = J^{-\frac{1}{3}}\mathbf{F} \tag{3}$$

with the determinant of the deformation gradient $J = \det \mathbf{F} > 0$, an isochoric part $\bar{\mathbf{F}}$ and a volumetric part $\mathbf{F}_{\text{vol}}$. Related deformation tensors, e.g. the unimod-

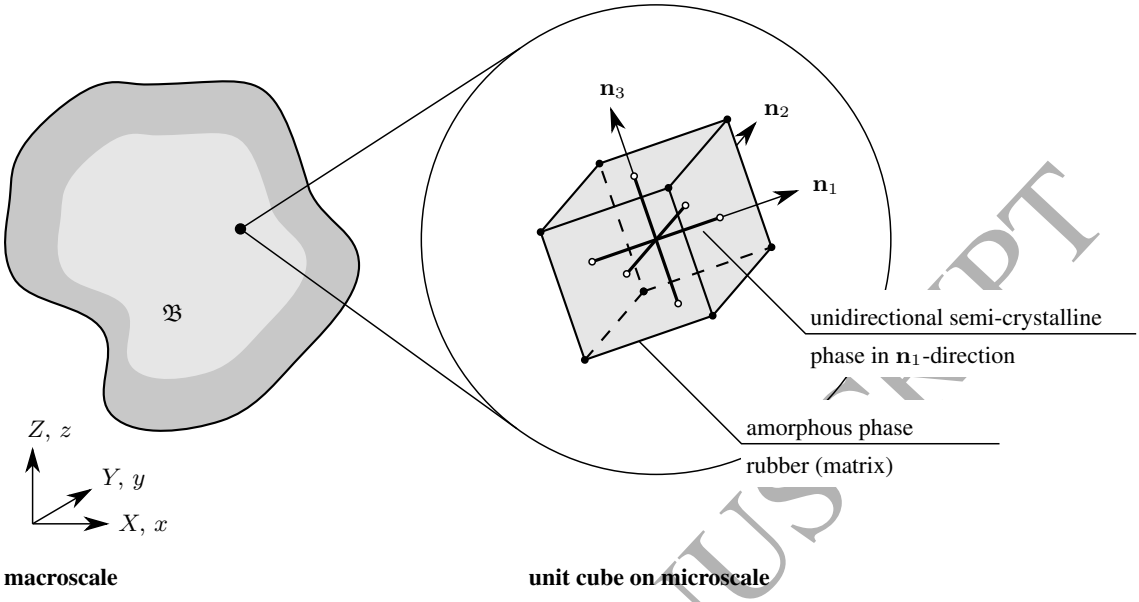

Figure 1: Macro- and microscale with representative volume element – unit cube

ular right Cauchy-Green deformation tensor

$$\overline{\mathbf{C}} = \overline{\mathbf{F}}^{\mathrm{T}}\,\overline{\mathbf{F}}\,, \tag{4}$$

are derived at the macro- and microscale. Volumetric and isochoric deformations are assumed as purely elastic (simplification for the sake of clarity to highlight the phenomena related to SIC in the following). As discussed e.g. in [33], other material features can be incorporated into the model if necessary (significant). The Helmholtz free energy per volume of the reference configuration is introduced as

$$\Psi_{\mathrm{am}} = \Psi_{\mathrm{EQ}} + \Psi_{\mathrm{NEQ}} \tag{5}$$

with an equilibrium part (ground state elasticity)

$$\Psi_{\mathrm{EQ}} = f_{\mathrm{EQ}}(\Theta)\left[\overline{\Psi}_0^e(\overline{\mathbf{C}}) + U_0(J)\right] + t(\Theta)\,e_{\mathrm{EQ},0} + \overline{\mathcal{C}}(\Theta) \tag{6}$$

ACCEPTED MANUSCRIPT

and a non-equilibrium part related to inelastic effects, e.g. viscoelasticity, which is neglected in this study for the sake of clarity, i.e.

$$\Psi_{\mathrm{NEQ}} = 0\,. \tag{7}$$

The equilibrium part of the Helmholtz free energy consists itself of energy density functions $\overline{\Psi}_0^e(\overline{\mathbf{C}})$ (isochoric part) and $U_0(J)$ (volumetric part), which are linked to the reference temperature Θ_0 for which $f_{\mathrm{EQ}}(\Theta_0) = 1$ holds. In the following, the index 0 denotes quantities related to the reference temperature Θ_0. A so-called temperature coefficient function $f_{\mathrm{EQ}}(\Theta)$ is used to represent the temperature dependency of the material (equilibrium branch). The term $\bar{\mathcal{C}}(\Theta)$ is a function of the deformation-independent heat capacity as well as the absolute temperature Θ and will be discussed in more detail in the following. The temperature function

$$t(\Theta) = 1 - \frac{\Theta}{\Theta_0} \tag{8}$$

describes in compact form the temperature dependency of the internal energy

$$e_{\mathrm{EQ},0} = \kappa_0\,\alpha_0\,\Theta_0\,\ln J\,, \tag{9}$$

itself evaluated at the reference temperature Θ_0. The terms κ_0 and α_0 denote the bulk modulus and the thermal volume expansion coefficient, respectively, evaluated at the reference temperature Θ_0. The simplest form of the temperature dependency is represented by the ansatz

$$f_{\mathrm{EQ}}(\Theta) = \frac{\Theta}{\Theta_0} \tag{10}$$

for the temperature coefficient function, which has been shown in detail by [34]. Note that also other temperature coefficient functions $f_{\mathrm{EQ}}(\Theta)$ are possible, for a

ACCEPTED MANUSCRIPT

general overview, it is referred to [34]. As energy density functions evaluated at the reference temperature Θ_0, the functions

$$U_0(J) = \kappa_0 \left(J - \ln(J) - 1\right) \tag{11}$$

and

$$\overline{\Psi}_0^e(\overline{\mathbf{C}}) = W^e(\bar{I}_1) + L^e(\bar{\lambda}_a) \tag{12}$$

are introduced, where the latter is assembled from the functions $W^e(\bar{I}_1)$ and $L^e(\bar{\lambda}_a)$ of the extended tube model proposed in [35] with

$$W^e(\bar{I}_1) = \frac{G_c}{2}\left[\frac{(1-\delta^2)\left(\bar{I}_1 - 3\right)}{1-\delta^2\left(\bar{I}_1 - 3\right)} + \ln\left(1-\delta^2\left(\bar{I}_1 - 3\right)\right)\right], \tag{13}$$

$$L^e(\bar{\lambda}_a) = \frac{2\,G_e}{\beta^2}\sum_{a=1}^{3}\left(\bar{\lambda}_a^{-\beta} - 1\right). \tag{14}$$

For the invariant $\bar{I}_1 = \operatorname{tr}\overline{\mathbf{C}} = \bar{\lambda}_1^2 + \bar{\lambda}_2^2 + \bar{\lambda}_3^2$ holds. G_c, G_e, β and δ are model parameters (shear modulus of chemical network nodes due to the crosslinks G_c, shear modulus of topological constraints G_e, chemical network parameter β, inextensibility of the network chains δ). For more details, the reader is referred to [35]. Furthermore, $\bar{\lambda}_a$ defines the principal stretch associated with the eigenvector $\mathbf{N}_a$ of the unimodular right Cauchy-Green tensor $\overline{\mathbf{C}}$ in the reference configuration,

$$\overline{\mathbf{C}} = \sum_{a=1}^{3} \bar{\lambda}_a^2\, \mathbf{N}_a \otimes \mathbf{N}_a\,. \tag{15}$$

The eigenvector $\mathbf{n}_a$ denotes its counterpart in the current configuration.

The general definition of the volumetric heat capacity of the material (amorphous phase)

$$c_{\text{am}} = -\Theta\,\frac{\partial^2 \Psi_{\text{am}}}{\partial\Theta\partial\Theta} \tag{16}$$

ACCEPTED MANUSCRIPT

per volume of the reference configuration is a function of the temperature- and deformation-dependent Helmholtz free energy function in terms of Ψ_{am}. According to the ansatz proposed in [34], Eq. (16) is expressed as

$$c_{\text{am}} = \bar{c}(\Theta) - \Theta \frac{\partial^2 g_{\text{EQ}}(\Theta)}{\partial\Theta\partial\Theta} \Psi_{\text{EQ},0} - \Theta \frac{\partial^2 g_{\text{NEQ}}(\Theta)}{\partial\Theta\partial\Theta} \Psi_{\text{NEQ},0} \,, \tag{17}$$

where in the present case

$$\bar{c}(\Theta) = c_0 \tag{18}$$

is introduced as constant ansatz for the volumetric heat capacity of the undeformed material in the model. For a temperature dependency of $\bar{c}(\Theta)$, it is referred to [36]. Furthermore, dimensionless functions $g_{\text{EQ}}(\Theta)$ and $g_{\text{NEQ}}(\Theta)$ are used to represent the dependency on temperature associated to the purely deformation-dependent energy terms $\Psi_{\text{EQ},0}$ and $\Psi_{\text{NEQ},0}$ evaluated at the reference temperature Θ_0. Since only the ground-state elasticity of the elastomer bulk material shall be considered, see Eq. (7), the non-equilibrium contribution in terms of $g_{\text{NEQ}}(\Theta)$ is omitted too and for the equilibrium contribution, the simple dimensionless function

$$g_{\text{EQ}}(\Theta) = \frac{\Theta}{\Theta_0} \tag{19}$$

is employed, which leads to the relation stated in Eq. (10) representing the simplest form of temperature dependency of the strain energy function in the context of thermo-elasticity, see also [37]. Note that also more sophisticated function types can be employed for $g_{\text{EQ}}(\Theta)$ and, in consequence, for $f_{\text{EQ}}(\Theta)$ in this framework if enough information on the temperature dependency of the material are available, e.g. from experiments. More details on the thermo-mechanical framework used are given in [34].

Finally, the term $\overline{\mathcal{C}}(\Theta)$ in Eq. (6) is addressed. For the further derivation, the function

$$\bar{g}(\Theta) = \frac{\bar{c}(\Theta)}{\Theta} \tag{20}$$

is introduced. An anti-derivative to $\bar{c}(\Theta)$ is computed by

$$\overline{C}(\tilde{\Theta}) = \int \bar{c}(\tilde{\Theta})\,\mathrm{d}\tilde{\Theta} \tag{21}$$

making use of Eq. (18). In the same manner, an anti-derivative

$$\overline{G}(\tilde{\Theta}) = \int \bar{g}(\tilde{\Theta})\,\mathrm{d}\tilde{\Theta} \tag{22}$$

is computed by making use of Eq. (20). After several computation steps, in analogy to the derivations presented in [34], the expression

$$\overline{\mathcal{C}}(\Theta) = \left[\overline{C}(\Theta) - \overline{C}(\Theta_0)\right] - \Theta\left[\overline{G}(\Theta) - \overline{G}(\Theta_0)\right] \tag{23}$$

of the Helmholtz free energy function Ψ_{EQ} of the equilibrium part from Eq. (6) can be completely specified. A more detailed description of the material model for the amorphous phase (also including continuum damage and finite thermo-viscoelasticity) is provided in [36].

2.3. Semi-crystalline phase

In Fig. 2, the relations related to SIC and observed from experimental measurements are illustrated in an idealized manner. From experiments (see e.g. [38]), the degree of crystallinity Φ depends on the applied stretch level λ_{s}. At small stretches, no significant SIC is observable. At moderate stretches, an onset of SIC takes place and SIC is mainly developed at large stretches only. A drop of the degree of crystallinity has been observed by increasing the temperature Θ. The growth and melting kinetics of SIC are time-dependent in general.

ACCEPTED MANUSCRIPT

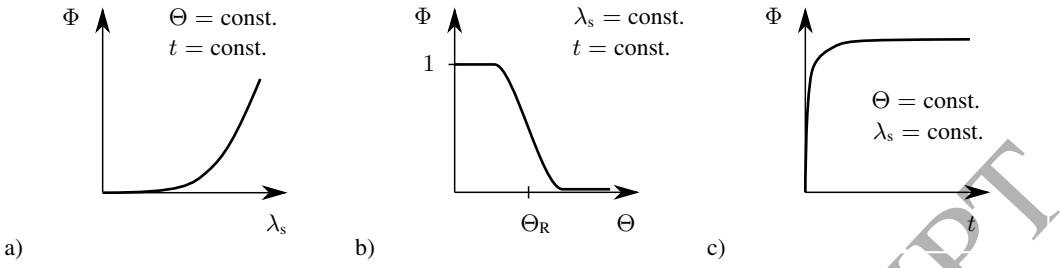

Figure 2: Idealized relations revealed from experimental observations, see e.g. [38], Figs. 3 and 4: a) degree of crystallinity as a function of stretch; b) degree of crystallinity as a function of temperature; c) degree of crystallinity as a function of time

If the stretch is kept constant, the degree of crystallinity reaches an equilibrium value with elapsing time.

To capture a potential reinforcement effect in all of the three principal stretch directions $\mathbf{n}_a$, three contributions $\Psi_{\text{cry}\,a}$ are considered,

$$\Psi_{\text{cry}} = \sum_{a=1}^{3} \Psi_{\text{cry}\,a} \,. \tag{24}$$

The semi-crystalline phase is characterized by a significant stiff and time-dependent deformation in terms of the associated free energy function

$$\Psi_{\text{cry}\,a} = \left[\frac{E_{\text{cry}}}{2} \left(\Phi_a^{\infty}(\lambda_{\text{s}}, \Theta) - \Phi_a \right)^2 + \Psi_{0\,a}^{\infty}(\lambda_{\text{s}}, \Theta) + \Delta h_{\text{r}} \left(1 - \Phi_a \right) \right] \tag{25}$$

$$\text{with} \quad \lambda_{\text{s}} = \lambda_a \,.$$

The free energy function is an ansatz consisting of three parts. $\Psi_{0\,a}^{\infty}(\lambda_{\text{s}})$ stands for the long-term free energy potential of semi-crystalline chains, i.e. evaluated at $t \to \infty$ and at the equilibrium degree of crystallinity $\Phi_a^{\infty}(\lambda_{\text{s}}, \Theta)$ with $\lambda_{\text{s}} \geq 1$. To take into account time-dependent effects of the SIC kinetics during cyclic dynamic loading, the energy term $E_{\text{cry}}/2 \left(\Phi_a^{\infty}(\lambda_{\text{s}}, \Theta) - \Phi_a \right)^2$ is added to take into account time-dependent crystal growth via the internal variable Φ_a representing

ACCEPTED MANUSCRIPT

ACCEPTED MANUSCRIPT

the current degree of crystallinity of semi-crystalline chains in the direction $\mathbf{n}_a$. The parameter E_{cry} represents the mechanical energy per volume of the reference configuration for crystal growth or melting. For the internal variable Φ_a, the evolution law

$$\dot{\Phi}_a = \frac{1}{\tau}\left[\Phi_a^{\infty}(\lambda_{\text{s}}, \Theta) - \Phi_a\right] \tag{26}$$

holds. The parameter τ models the time characteristics of crystal growth (τ_{l}) and melting (τ_{unl}). For $\tau_{\text{unl}} \to 0$, instantaneous melting of the crystallites would be represented. Different parameters τ_{l} and τ_{unl} take into account time differences in the crystal growth and melting kinetics. Note that Eq. (26) represents a phenomenological approach, however, which is in good qualitative agreement with experimental observations previously published e.g. in [38], where crystal growth and melting are driven by the current difference of the current degree of crystallinity Φ_a to the current long-term value $\Phi_a^{\infty}(\lambda_{\text{s}}, \Theta)$. The proposed model is illustrated in Fig. 4. More advanced diffusion models have been discussed in the literature. These models are partially based on more physical considerations but are also fitted to experimentally observed relations via a priori unknown model parameters. Regarding the time dependency of SIC during unloading, a nearly instantaneous melting of crystallites has been reported from experiments, see e.g. [13]. Hence, melting of crystallites takes place much faster than crystal growth. The third part in Eq. (25) takes into account the contribution of the exothermic chemical reaction of crystal growth (assumed as fully reversible). Hence, the parameter Δh_{r} stands for the part of heat energy reversibly released during the complete transformation from amorphous to crystalline phase (release of latent heat), see [19]. Additionally during crystal growth and melting, mechanical energy from the stress field is continuously transformed to heat energy

resulting in a dissipative material behavior due to SIC

$$-\frac{\partial \Psi_{\text{cry}\,a}}{\partial \Phi_a}\,\dot{\Phi}_a - \frac{1}{\Theta}\,\mathbf{Q}\cdot\nabla_{\mathbf{X}}\Theta \geq 0 \tag{27}$$

(remaining part of the second law of thermodynamics – Clausius-Duhem inequality). Eq. (27) contains a heat flux contribution with the heat flux vector $\mathbf{Q}$ (reference configuration) for which Fourier's law will be used. Furthermore, to fulfill the dissipation inequality with respect to the part of the internal variable Φ_a (thermodynamical consistency), the ansatz

$$\begin{aligned}\dot{\Phi}_a &= -\dot{\gamma}\,\frac{\partial \Psi_{\text{cry}\,a}}{\partial \Phi_a} \\ &= -\frac{1}{\tau\,E_{\text{cry}}}\left\{-E_{\text{cry}}\left[\Phi_a^{\infty}(\lambda_{\text{s}},\Theta)-\Phi_a\right]\right\}\end{aligned} \tag{28}$$

is used, which results in the evolution law stated in Eq. (26) with

$$\dot{\gamma} = \frac{1}{\tau\,E_{\text{cry}}} \geq 0\,. \tag{29}$$

In other words, the current degree of crystallinity Φ_a is used as an internal variable (history variable) to numerically take into account rate- and temperature-dependent SIC processes of crystal growth and melting over time. Note that the part $\Delta h_{\text{r}}\,(1-\Phi_a)$ does not contribute to an additional stress response, since Δh_{r} is assumed as deformation- and temperature-independent (constant).

For the reference equilibrium degree of crystallinity, the positive function

$$\Phi_a^{\infty}(\lambda_{\text{s}},\Theta) = f_{\text{cry}}(\Theta)\,\frac{1}{2}\left(\tanh(\lambda_{\text{s}}-\lambda_{\text{cry}})+1\right) \quad \text{with} \quad \lambda_{\text{s}}=\lambda_a \geq 1 \tag{30}$$

is used, where $f_{\text{cry}}(\Theta) \leq 1$ is a temperature function describing the maximum degree of crystallinity at the temperature Θ and $\lambda_{\text{cry}} \geq 1$ describes the onset of pronounced SIC effects with respect to the stretch λ_{s}.

ACCEPTED MANUSCRIPT

ACCEPTED MANUSCRIPT

The long-term reference free energy contribution of the semi-crystalline phase depends on the applied stretch λ_s and the current temperature Θ via the temperature dependency of the degree of crystallinity,

$$\Psi^{\infty}_{0\,a}(\lambda_\mathrm{s},\Theta) = f_\mathrm{cry}(\Theta)\,\frac{G_\mathrm{cry}}{48}\left(\lambda_\mathrm{s}^2-1\right)^4 \quad \text{with} \quad \lambda_\mathrm{s}=\lambda_a\geq 1\,, \tag{31}$$

where G_cry represents a material parameter describing the stiffness of the evolving semi-crystalline phase and $\lambda_\mathrm{s}=\lambda_a\geq 1$ is the stretch in the direction $\mathbf{n}_a$ of the SIC evolution process. For compression states of the amorphous phase, i.e. $\lambda_\mathrm{s}<1$, the free energy function is set to zero. Furthermore, the temperature evolution function of the semi-crystalline phase is introduced as simple as possible with

$$f_\mathrm{cry}(\Theta) = \frac{1}{2}\left[1-\tanh(b\,(\Theta-\Theta_\mathrm{R}))\right]. \tag{32}$$

Near the reference temperature Θ_R, the proposed temperature coefficient function given in Eq. (32) shows a nearly linear temperature dependency (slope $-0.5\,b$). The slope in terms of $-0.5\,b$ around the temperature Θ_R can be identified from experimental studies involving temperature changes for SIC processes, previously performed and published e.g. in [38] or in [39]. In these studies, the degree of crystallinity at constant strain level decreases with increasing temperature, nearly linear proportional to temperature. Note that the negative slope of the temperature coefficient function given in Eq. (32) results in an energy-elastic solid-like behavior (cooling upon stretching) of the material portion described by the second term in Eq. (25), i.e. $\Psi^{\infty}_{0\,a}(\lambda_\mathrm{s},\Theta)$.

The functions defined in Eqs. (30) and (32) are illustrated in Fig. 3. A model representation of the semi-crystalline phase upon stretching is given in Fig. 4. Note that in case of vanishing time dependency (equilibrium state of crystallization at constant stretch and temperature), a direct relation between λ_s and

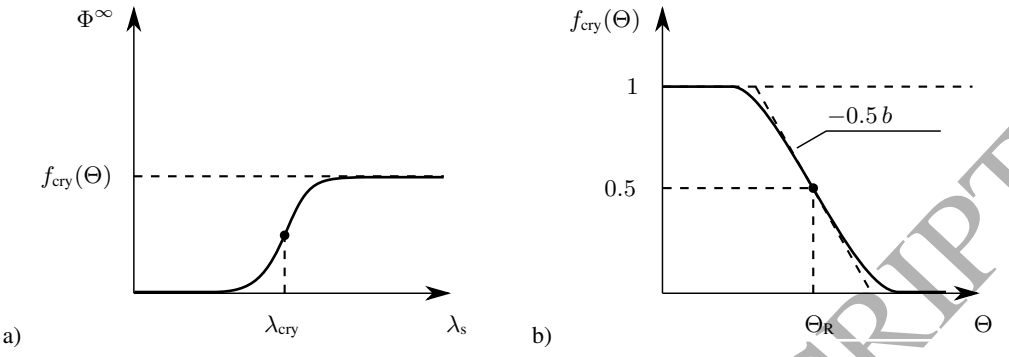

Figure 3: Model representation of the long-term degree of crystallinity Φ^∞: a) as a function of the stretch λ_{s}; b) as a function of the absolute temperature Θ

the associated long-term value $\Phi_a^\infty(\lambda_{\text{s}}, \Theta)$ can be established, i.e. the degree of crystallinity is not an argument of the function given in Eq. (31).

From the previously mentioned relations, the stress contribution in the form of the scalar second Piola-Kirchhoff stress of the semi-crystalline phase is

$$\begin{aligned} S_{\text{cry}\,a} &= 2\,\frac{\partial \Psi_{\text{cry}\,a}}{\partial \lambda_{\text{s}}^2} \\ &= \left[H_a + \left\{ f_{\text{cry}}(\Theta)\,\frac{G_{\text{cry}}}{6}\left(\lambda_{\text{s}}^2 - 1\right)^3 \right\} \right] \quad \text{with} \quad \lambda_{\text{s}} = \lambda_a \geq 1\,, \end{aligned} \tag{33}$$

where the non-equilibrium stress due to crystal growth or melting is

$$\begin{aligned} H_a &= 2\,E_{\text{cry}}\left[\Phi_a^\infty(\lambda_{\text{s}}, \Theta) - \Phi_a\right] \frac{\partial \Phi_a^\infty(\lambda_{\text{s}}, \Theta)}{\partial \lambda_{\text{s}}^2} \quad \text{with} \quad \lambda_{\text{s}} = \lambda_a \geq 1 \\ &= 2\,E_{\text{cry}}\left[\Phi_a^\infty(\lambda_{\text{s}}, \Theta) - \Phi_a\right] f_{\text{cry}}(\Theta)\,\frac{1}{2}\left(1 - \tanh^2(\lambda_{\text{s}} - \lambda_{\text{cry}})\right) \frac{1}{2\,\lambda_{\text{s}}} \end{aligned} \tag{34}$$

and the scalar tangent moduli (reference configuration)

$$C_{\text{cry}\,a} = 2\,\frac{\partial S_{\text{cry}\,a}}{\partial \lambda_{\text{s}}^2} \quad \text{with} \quad \lambda_{\text{s}} = \lambda_a \geq 1 \tag{35}$$

can be computed. In the following, some aspects on the FE implementation, especially for the semi-crystalline phase, are provided.

ACCEPTED MANUSCRIPT

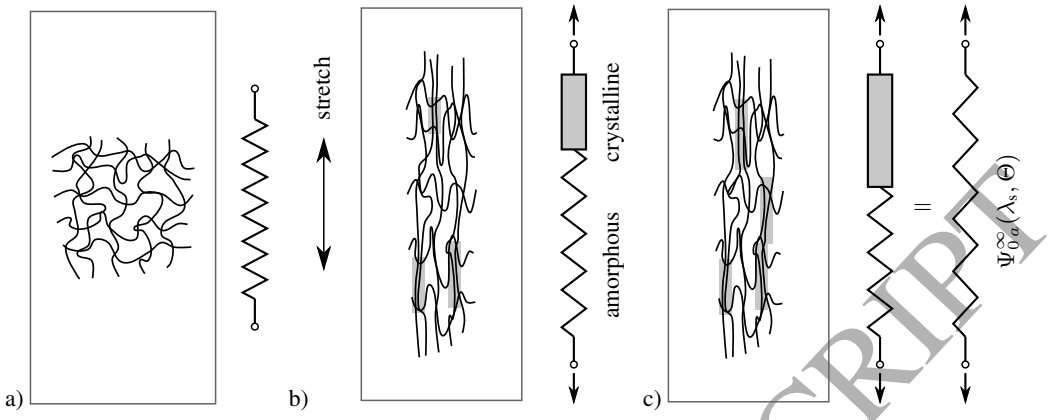

Figure 4: Model representation of semi-crystalline phase upon stretching: a) unstretched amorphous rubber; b) significantly stretched rubber with first crystalline domains (rigid) after initial loading; c) long-term state of semi-crystalline rubber at constant stretch – free energy of remaining amorphous part represented by $\Psi_{0\,a}^{\infty}(\lambda_s, \Theta)$

Finally, the semi-crystalline phase contributes to the volumetric heat capacity of the two-phase material via the additional part

$$c_{\text{cry}} = -\Theta \frac{\partial^2 \Psi_{\text{cry}}}{\partial \Theta \partial \Theta} \tag{36}$$

per volume of the reference configuration in analogy to Eq. (16). Note that this part depends on deformation and temperature as well but vanishes for a fully amorphous, undeformed material state. The contributions from both phases (amorphous and semi-crystalline) are combined during the FE assembling process, which is addressed in more detail in the following subsection.

2.4. Finite element implementation and unidirectional strain-induced reinforcement effect

The solution of the evolution equation stated in Eq. (26) is given in terms of an update formula (at time $t_{n+1} = t_n + \Delta t$) for crystal growth ($\Phi_a^{\infty}(\lambda_s, \Theta) - \Phi_a \geq$

ACCEPTED MANUSCRIPT

ACCEPTED MANUSCRIPT

0)

$$\Phi_a^{t_{n+1}} = \left(1 + \frac{\tau_\mathrm{l}}{\Delta t}\right)^{-1} \left(\Phi_a^\infty(\lambda_\mathrm{s}, \Theta)^{t_{n+1}} + \frac{\tau_\mathrm{l}}{\Delta t}\, \Phi_a^{t_n}\right) \quad \text{with} \quad \lambda_\mathrm{s} = \lambda_a \quad (37)$$

and melting ($\Phi_a^\infty(\lambda_\mathrm{s}, \Theta) - \Phi_a < 0$)

$$\Phi_a^{t_{n+1}} = \left(1 + \frac{\tau_\mathrm{unl}}{\Delta t}\right)^{-1} \left(\Phi_a^\infty(\lambda_\mathrm{s}, \Theta)^{t_{n+1}} + \frac{\tau_\mathrm{unl}}{\Delta t}\, \Phi_a^{t_n}\right) \quad \text{with} \quad \lambda_\mathrm{s} = \lambda_a \,. \quad (38)$$

Eqs. (37) and (38) describe the time evolution function of crystal growth and melting in the considered direction $\mathbf{n}_a$.

From the weak form of the balance of momentum

$$G_m(\mathbf{u}) = \int_\mathfrak{B} \mathbf{S} \cdot \delta\mathbf{E}\, \mathrm{d}V - \int_\mathfrak{B} \rho_0 \left(\mathbf{b}_0 - \ddot{\mathbf{u}}\right) \cdot \mathbf{u}\, \mathrm{d}V - \int_{\partial\mathfrak{B}} \mathbf{T} \cdot \mathbf{u}\, \mathrm{d}A = 0 \quad (39)$$

and the weak form of the balance of energy

$$G_t(\delta\Theta) = \int_\mathfrak{B} \left(w_\mathrm{am} - c_\mathrm{am}\, \dot{\Theta}\right) \delta\Theta\, \mathrm{d}V + \int_\mathfrak{B} \mathbf{Q} \cdot \nabla_\mathbf{X} \left(\delta\Theta\right) \mathrm{d}V - \int_{\partial\mathfrak{B}} \mathbf{Q} \cdot \mathbf{N}\, \delta\Theta\, \mathrm{d}A \,, \quad (40)$$

the FE formulation of a thermo-mechanically coupled solid element (amorphous phase), see Fig. 5, can be derived as outlined e.g. in [40]. $\mathbf{S}$ denotes the second Piola-Kirchhoff stress tensor, $\mathbf{E}$ stands for the Green-Lagrange strain tensor, ρ_0 is the mass density in the reference configuration, $\mathbf{b}_0$ are volume forces due to gravity and $\mathbf{T}$ are surface tractions in the reference configuration. The weak form of the balance of energy also contains internal and external work contributions in terms of w_am, the heat capacity c_am and heat flux vector $\mathbf{Q}$ of the amorphous phase in the reference configuration.

The representative solid element in Fig. 5 contains the afore-introduced uni-directional SIC reinforcement in the three principal stretch directions along the vectors $\mathbf{n}_a$, see also Fig. 1, as additional finite elements in the form of rebars at

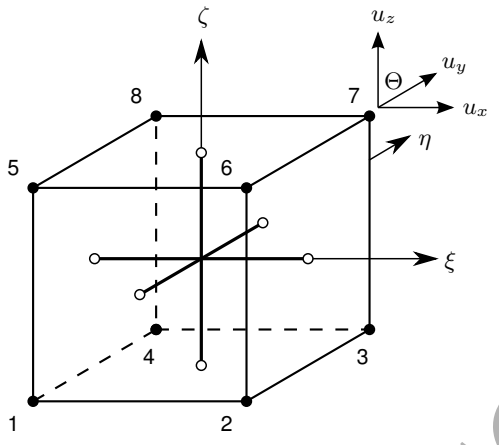

Figure 5: Solid 8-node finite element (unit cube) with three displacement (u_x, u_y, u_z) degrees of freedom and one temperature (Θ) degree of freedom per node (dimensions for the examples investigated, see Sections 3 and 4, are 1 mm $\times$ 1 mm $\times$ 1 mm)

large deformations, see e.g. [41] for an isothermal formulation at large strains. In the following, the FE formulation for one of the three thermo-mechanically coupled rebars is discussed in more detail.

In Fig. 6, a thermo-mechanical 2-node rebar element is considered for the direction $\mathbf{n}_a$. The rebar element is formed by the vector linking the two nodes 1 and 2 in longitudinal s-direction of the rebar. In the reference configuration, the distance (length) between the two nodes is

$$L = \sum_{i=1}^{3} \left(X_{i,2} - X_{i,1}\right)^2 . \tag{41}$$

$X_{i,j}$ denotes the nodal coordinate in the reference configuration in the i-th direction at node j of the rebar element. A local coordinate system can be associated with the rebar element considered. With the help of this local coordinate system, the rebar stretches (principal stretches) λ_{s}, λ_{q1} and λ_{q2} are measured. λ_{s} denotes the longitudinal stretch in rebar direction, while λ_{q1} and λ_{q2} are associated with the stretches perpendicular to the longitudinal direction. The principal stretches

ACCEPTED MANUSCRIPT

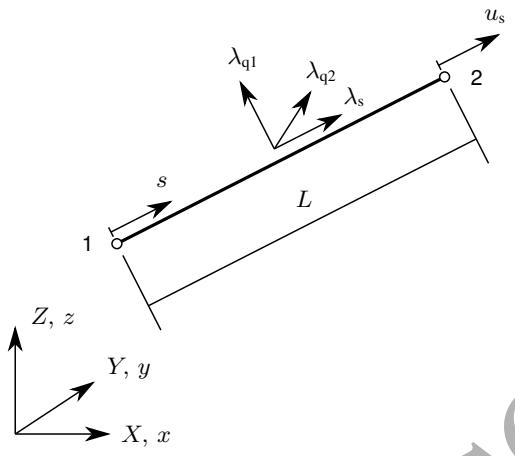

Figure 6: 2-node rebar element arbitrarily orientated in the 3D space

of the rebar element can be computed from the current and the initial position of the rebar element in the current configuration and the reference configuration, respectively. The current positions of the nodes are expressed in terms of the nodal displacements $\mathbf{u}$. The current length l is

$$l = L + u = \sqrt{\sum_{i=1}^{3} [(X_{i,2} + u_{i,2}) - (X_{i,1} + u_{i,1})]^2}. \tag{42}$$

The principal stretch in rebar direction can be computed from the current length l,

$$\lambda_\mathrm{s} = \frac{l}{L}. \tag{43}$$

For the constitutive, unidirectional material behavior of the rebar, incompressible material behavior shall be assumed, i.e.

$$J_\mathrm{r} = \lambda_\mathrm{s}\, \lambda_{\mathrm{q}1}\, \lambda_{\mathrm{q}2} = \lambda_\mathrm{s}\, \lambda_\mathrm{q}^2 = 1 \tag{44}$$

with equal lateral stretches $\lambda_{\mathrm{q}1} = \lambda_{\mathrm{q}2} = \lambda_\mathrm{q}$,

$$\lambda_\mathrm{q} = \frac{1}{\sqrt{\lambda_\mathrm{s}}}. \tag{45}$$

ACCEPTED MANUSCRIPT

ACCEPTED MANUSCRIPT

From this assumption, the lateral stresses of the rebar are zero. The longitudinal Green-Lagrange strain of the rebar is

$$E_{\mathrm{s}} = \frac{1}{2}\left(\lambda_{\mathrm{s}}^2 - 1\right). \tag{46}$$

According to the weak forms of the solid amorphous phase given in Eqs. (39) and (40), the weak form of the balance of momentum for the rebar element is given by

$$G_m = \int_{(s)} \delta E_{\mathrm{s}}\, S_{\mathrm{cry}}\, A \,\mathrm{d}s - \int_{(s)} \delta u\, b\, A \,\mathrm{d}s - \sum_k \delta u_k\, P_k = 0, \tag{47}$$

with b denoting the volume force and P_k are nodal forces at the node k. The weak form of the balance of energy results in

$$G_t = \int_{(s)} \left(w_{\mathrm{cry}} - c_{\mathrm{cry}}\,\dot{\Theta}\right) \delta\Theta\, A \,\mathrm{d}s + \int_{(s)} Q\, \nabla_{\mathbf{X}}\left(\delta\Theta\right) A \,\mathrm{d}s - \int_{\partial V} \mathbf{Q}\cdot\mathbf{N}\, \delta\Theta \,\mathrm{d}A \tag{48}$$

The scalar heat flux along the rebar direction is obtained using Fourier's law

$$Q = -k_{\mathrm{cry}}\, \frac{1}{\lambda^2}\, \nabla_{\mathbf{X}}\left(\Theta\right) \tag{49}$$

with the heat conduction coefficient $k_{\mathrm{cry}} \geq 0$ along the reinforcement direction. Note that values of $k_{\mathrm{cry}} > 0$ will lead to an additional heat conduction in the direction considered (anisotropic) apart from the heat conduction of the underlying amorphous phase (isotropic). If crystallized domains are not connected to each other, i.e. if they are surrounded by amorphous domains, the additional effect of SIC on the heat conduction will be less significant (connection in series).

The work $w_{\mathrm{cry}} = w_{\mathrm{int}} + w_{\mathrm{ext}}$ consists of the internal work contribution

$$w_{\mathrm{int}} = -\left(\frac{\partial \Psi_{\mathrm{cry}}}{\partial \Phi} - \Theta\, \frac{\partial^2 \Psi_{\mathrm{cry}}}{\partial \Theta\, \partial \Phi}\right) \dot{\Phi} \tag{50}$$

and the external work contribution

$$w_{\text{ext}} = \Theta \, \frac{\partial S_{\text{cry}}}{\partial \Theta} \, \dot{E}_{\text{s}} \tag{51}$$

of the semi-crystalline phase (rebars). With the help of the weak form of the balance equations, a consistent linearization can be performed around a known solution point denoted by the index p at time t_n,

$$G_m(\mathbf{u}_p + \Delta\mathbf{u}, \boldsymbol{\Theta}_p + \Delta\boldsymbol{\Theta}) \approx G_m(\mathbf{u}_p, \boldsymbol{\Theta}_p) + \left.\frac{\partial G_m}{\partial \mathbf{u}}\right|_p \Delta\mathbf{u} + \left.\frac{\partial G_m}{\partial \boldsymbol{\Theta}}\right|_p \Delta\boldsymbol{\Theta} \,, \tag{52}$$

and in analogy

$$G_t(\mathbf{u}_p + \Delta\mathbf{u}, \boldsymbol{\Theta}_p + \Delta\boldsymbol{\Theta}) \approx G_t(\mathbf{u}_p, \boldsymbol{\Theta}_p) + \left.\frac{\partial G_t}{\partial \mathbf{u}}\right|_p \Delta\mathbf{u} + \left.\frac{\partial G_t}{\partial \boldsymbol{\Theta}}\right|_p \Delta\boldsymbol{\Theta} \,. \tag{53}$$

Reordering allows to formulate a system of linear equations in the form

$$\begin{bmatrix} \left.\frac{\partial G_m^e}{\partial \mathbf{u}}\right|_p & \left.\frac{\partial G_m^e}{\partial \boldsymbol{\Theta}}\right|_p \\ \left.\frac{\partial G_t^e}{\partial \mathbf{u}}\right|_p & \left.\frac{\partial G_t^e}{\partial \boldsymbol{\Theta}}\right|_p \end{bmatrix} \begin{bmatrix} \Delta\mathbf{u}^e \\ \Delta\boldsymbol{\Theta}^e \end{bmatrix} = \begin{bmatrix} -G_m^e(\mathbf{u}_p^e, \boldsymbol{\Theta}_p^e) \\ -G_t^e(\mathbf{u}_p^e, \boldsymbol{\Theta}_p^e) \end{bmatrix} , \tag{54}$$

which has to be solved with respect to the unknown vector containing the increments in nodal displacements $\mathbf{u}^e$ and nodal temperatures $\boldsymbol{\Theta}^e$ to obtain the new solution at time t_{n+1}. Eq. (54) can be abbreviated as

$$\begin{bmatrix} \mathbf{S}_{uu} & \mathbf{S}_{u\Theta} \\ \mathbf{S}_{\Theta u} & \mathbf{S}_{\Theta\Theta} \end{bmatrix} \begin{bmatrix} \Delta\mathbf{u}^e \\ \Delta\boldsymbol{\Theta}^e \end{bmatrix} = \begin{bmatrix} \mathbf{r}_1 \\ \mathbf{r}_2 \end{bmatrix} \tag{55}$$

with the terms

$$\mathbf{S}_{uu} = \begin{bmatrix} (\mathbf{A}_1 + \mathbf{A}_2) & -(\mathbf{A}_1 + \mathbf{A}_2) \\ -(\mathbf{A}_1 + \mathbf{A}_2) & (\mathbf{A}_1 + \mathbf{A}_2) \end{bmatrix} , \tag{56}$$

$$\mathbf{S}_{u\Theta} = \begin{bmatrix} -\mathbf{C}_1 & -\mathbf{C}_1 \\ \mathbf{C}_1 & \mathbf{C}_1 \end{bmatrix} , \tag{57}$$

ACCEPTED MANUSCRIPT

$$\mathbf{S}_{\Theta u} = \begin{bmatrix} \mathbf{D}_1 - \mathbf{D}_2 & -\mathbf{D}_1 + \mathbf{D}_2 \\ -\mathbf{D}_1 - \mathbf{D}_2 & \mathbf{D}_1 + \mathbf{D}_2 \end{bmatrix} \tag{58}$$

and

$$\mathbf{S}_{\Theta\Theta} = \begin{bmatrix} -B_1 - B_2 + B_3 & B_1 - B_2 + B_3 \\ B_1 - B_2 + B_3 & -B_1 - B_2 + B_3 \end{bmatrix}. \tag{59}$$

The derivation of the matrix components from Eqs. (55) to (59) is shown and given in Appendix A. Note that up to this stage, Eq. (55) abbreviated as

$$\mathbf{S}_{\mathrm{r}}\, \Delta\mathbf{u}_{\mathrm{r}} = \mathbf{r}_{\mathrm{r}} \tag{60}$$

is formulated with respect to the nodes of the thermo-mechanically coupled rebar element sketched in Fig. 6,

$$\begin{bmatrix} \Delta\mathbf{u}^e \\ \Delta\boldsymbol{\Theta}^e \end{bmatrix} = \begin{bmatrix} \Delta u^e_{1,1} & \Delta u^e_{2,1} & \Delta u^e_{3,1} & \Delta u^e_{1,2} & \Delta u^e_{2,2} & \Delta u^e_{3,2} & \Delta\Theta^e_1 & \Delta\Theta^e_2 \end{bmatrix}^{\mathrm{T}}. \tag{61}$$

As illustrated in Fig. 5, the nodal unknowns of the rebar element in each principal stretch direction are projected to the nodes of the underlying solid element of the amorphous phase. The link between the displacement degrees of freedom of the rebar element $\mathbf{u}^e_{\mathrm{r}}$ and the solid element $\mathbf{u}^e$ is formed by the reduction matrix $\mathbf{R}$,

$$\mathbf{u}^e_{\mathrm{r}} = \mathbf{R}\,\mathbf{u}^e, \tag{62}$$

$$\begin{bmatrix} \mathbf{u}^1 \\ \mathbf{u}^2 \end{bmatrix} = \begin{bmatrix} \mathbf{N}_8(\xi_1, \eta_1, \zeta_1) \\ \mathbf{N}_8(\xi_2, \eta_2, \zeta_2) \end{bmatrix} \begin{bmatrix} \mathbf{u}^e \end{bmatrix} \tag{63}$$

with the shape functions N_i of the 8-node solid element evaluated at the positions of the node 1 and 2 of the rebar element (ξ_1, η_1, ζ_1) and (ξ_2, η_2, ζ_2), respectively.

ACCEPTED MANUSCRIPT

ACCEPTED MANUSCRIPT

Hence, the reduction matrix takes the form

$$\mathbf{R} = \begin{bmatrix} \mathbf{N}_8(\xi_1, \eta_1, \zeta_1) \\ \mathbf{N}_8(\xi_2, \eta_2, \zeta_2) \end{bmatrix} \tag{64}$$

with the 3×3 identity matrix $\mathbf{I}$,

$$\mathbf{N}^8(\xi_i, \eta_i, \zeta_i) = \begin{bmatrix} \mathbf{I}\, N_1(\xi_i, \eta_i, \zeta_i) & \dots & \mathbf{I}\, N_8(\xi_i, \eta_i, \zeta_i) \end{bmatrix}. \tag{65}$$

The additional (mechanical) contribution of the semi-crystalline phase to the representative solid element is in this case

$$\mathbf{R}^{\mathrm{T}}\, \mathbf{S}_{\mathrm{r}}^{e}\, \mathbf{R}\, \Delta\mathbf{u}^{e} = \mathbf{R}^{\mathrm{T}}\, \mathbf{r}_{\mathrm{r}}^{e}\,, \tag{66}$$

$$\mathbf{S}^{e}\, \Delta\mathbf{u}^{e} = \mathbf{r}^{e} \tag{67}$$

in terms of the nodal displacement unknowns of the solid element. The reduction matrix for the temperature degrees of freedom is established in analogy.

In the following, the proposed model for time- and temperature-dependent SIC is applied to the analysis of rubber specimens under tensile loading and a steady state rolling tire with a pronounced dynamic load pattern.

3. Comparison to experimental observations

In this section, several features of the proposed model for time- and temperature-dependent SIC are highlighted. Model parameters are identified from tensile experiments previously investigated in [24] and in [39].

3.1. Tensile test

As first example, the proposed model for time- and temperature-dependent SIC is applied to the analysis of a sulfur vulcanized NR (NR-S) specimen loaded

ACCEPTED MANUSCRIPT

and unloaded in tensile mode. The experiment and its results are documented in [24], where also further details regarding the material formulation and cure conditions are provided. First, the specimen was placed in a thermal chamber at $0°$C. The strain rate was $5.5 \cdot 10^{-3}$ s^{-1}. According to [24], time-resolved WAXD patterns and simultaneous stress-stretch relations were continuously recorded (no holding times during loading and unloading). Information on the current temperature state of the specimen were not recorded during the experiment.

The model parameters to simulate the material response seen from the experiment are given in Tab. 1. The model parameters have been identified by fitting the simulation outcome to the experimentally measured data provided in [24] based on further information from [35] and standard values for rubber material from the literature, see e.g. [42] (thermal properties). For the thermo-mechanically coupled simulation, no heat exchange with the environment is considered (thermally insulated specimen) for the sake of simplicity. The time step size for the simulation is $\Delta t = 1.0$ s.

In Fig. 7, the computed stress-stretch relation, the evolution of the degree of crystallinity as well as the temperature variation as a function of the current stretch in tensile direction are provided together with the experimental data if applicable. Note that the stress reduction (plateau) at the onset of SIC in NR, see e.g. [39], is neglected by the model. For comparison, the result of the numerical study assuming an identical non-crystallizing rubber (purely amorphous upon loading) is also plotted in Fig. 7. It can be observed that due to time-dependent SIC kinematics, a hysteresis is formed by the loading and unloading path of the specimen in the stress-stretch plot giving rise to a remaining temperature increase (dissipation of mechanical input energy) after unloading of the specimen, see Fig. 7 c). In general, unfilled rubber behaves like an entropy-elastic solid

ACCEPTED MANUSCRIPT

Table 1: Model parameters for amorphous and semi-crystalline phase: tensile test according to [24] ($T = 0°\text{C}$)

G_c	[MPa]	0.355
δ	$[-]$	0.09693
G_e	[MPa]	0.351
β	$[-]$	0.2
Θ_0	[K]	273.0
k	$\left[\frac{\text{W}}{\text{m K}}\right]$	0.235
c_0	$\left[\frac{\text{MPa}}{\text{K}}\right]$	1.439
α_V	$\left[\text{K}^{-1}\right]$	0.00048
ρ_0	$\left[\frac{\text{g}}{\text{cm}^3}\right]$	1.10
G_{cry}	[MPa]	0.0005
τ_{l}	[s]	190.0
τ_{unl}	[s]	τ_{l}
A	$\left[\text{mm}^2\right]$	1.0
Θ_{R}	[K]	155.0
b	$[-]$	0.005
E_{cry}	[MPa]	100.0
λ_{cry}	$[-]$	4.5
k_{cry}	$\left[\frac{\text{W}}{\text{m K}}\right]$	0.235
Δh_{r}	[MPa]	50.0

ACCEPTED MANUSCRIPT

below the onset of SIC, i.e. reversible heating and cooling upon stretching and unloading occurs, respectively. Heat of crystallization (release of latent heat) contributes to a further heating during crystal growth. Melting of crystallites results in a cooling. The thermal consequences of these mainly reversible chemical reactions are incorporated into the model via the additional chemical energy term $\Delta h_{\mathrm{r}}\,(1-\Phi_a)$, see (25). SIC above a material-specific stretch level does not lead to a further heating upon stretching but to a slight cooling (energy-elastic material behavior) as it can be observed in Fig. 7 c). Nevertheless, the thermal short-term and long-term effects and underlying mechanisms of SIC, especially for cyclic loading conditions, are still under debate [43, 31, 32, 44].

The further increase of the degree of crystallinity at the start of the unloading process, see Fig. 7 b), is a direct outcome of the assumed evolution law (SIC kinetics). Since the equilibrium (maximum) degree of crystallinity was not reached by the current value of the degree of crystallinity during loading (time dependency), the driving force on the crystallization is still large enough to stimulate a further increase at the beginning of unloading. However, at a certain stretch level, the associated equilibrium (maximum) degree of crystallinity becomes smaller than the current value and, in consequence, melting of crystallites starts.

From a physical point of view, a relation between G_{cry}, E_{cry}, Δh_{r} and the parameters of the amorphous phase can be established by polymer physical considerations since the reinforcing effect originates from the stretched amorphous phase.

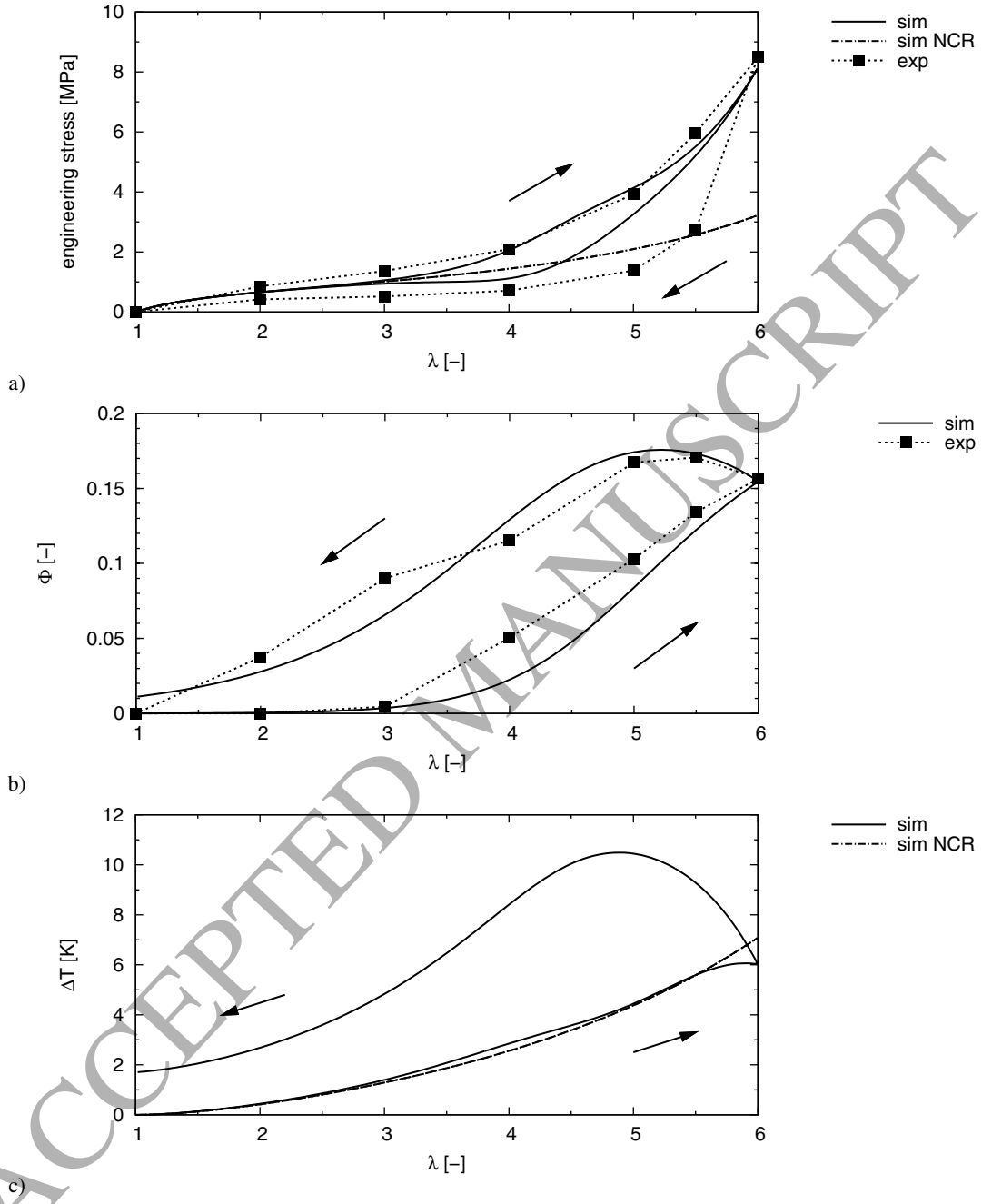

Figure 7: Tensile experiment – loading and unloading (strain rate $5.5 \cdot 10^{-3}$ s^{-1}) at initial temperature $T = 0°C$ (experimental data (exp), see [24], and simulation for strain-crystallizing rubber (sim) and for non-crystallizing rubber (sim NCR) for comparison): a) engineering stress as a function of stretch λ ; b) degree of crystallinity as a function of stretch λ; c) temperature variation as a function of stretch λ

ACCEPTED MANUSCRIPT

ACCEPTED MANUSCRIPT

3.2. Strain-induced crystallization and role of temperature

As second example, the proposed model for time- and temperature-dependent SIC is used to highlight the role of the testing temperature on the degree of crystallization and the stress response of a sulfur vulcanized NR specimen loaded and unloaded in tensile mode. The experiment and its results are documented in [39], where also further details regarding the material formulation and testing are provided. First, specimens were placed in a thermal chamber at $11°$C, $33°$C, $52°$C and $72°$C, respectively. Second, a constant strain rate of $1.117 \cdot 10^{-3}$ s^{-1} was applied for loading and unloading. According to [39], time-resolved synchrotron measurements and simultaneous stress-stretch relations were continuously recorded (no holding times during loading and unloading). Information on the current temperature state (deformation-induced temperature change) of the specimen were not recorded during the experiment.

The model parameter set to simulate the material response seen from the experiment is given in Tab. 2 and represents the material behavior for the temperature range considered. The model parameters have been identified by fitting the simulation outcome to the experimentally measured data provided in [39] and standard values for rubber material from the literature, see e.g. [42] (thermal properties). For the thermo-mechanically coupled simulation, no heat exchange with the environment is considered (thermally insulated specimen) for the sake of simplicity. The time step size for the simulation is $\Delta t = 5.0$ s.

In Fig. 8, the computed stress-stretch relation and the evolution of the degree of crystallinity as a function of the current stretch in tensile direction are provided together with the experimental data. It can be observed that due to time-dependent SIC kinematics, a hysteresis is formed by the loading and unloading path of the specimen in the stress-stretch plot for lower temperatures at which

Table 2: Model parameters for amorphous and semi-crystalline phase: tensile test according to [39] ($T = 11°\text{C}$, $T = 33°\text{C}$, $T = 52°\text{C}$, $T = 72°\text{C}$)

G_c	[MPa]	0.195
δ	$[-]$	0.09693
G_e	[MPa]	0.321
β	$[-]$	0.2
Θ_0	[K]	284.0
k	$\left[\frac{\text{W}}{\text{m K}}\right]$	0.235
c_0	$\left[\frac{\text{MPa}}{\text{K}}\right]$	1.439
α_V	$\left[\text{K}^{-1}\right]$	0.00048
ρ_0	$\left[\frac{\text{g}}{\text{cm}^3}\right]$	1.10
G_{cry}	[MPa]	0.0001
τ_{l}	[s]	300.0
τ_{unl}	[s]	τ_{l}
A	$\left[\text{mm}^2\right]$	1.0
Θ_{R}	[K]	255.0
b	$[-]$	0.016
E_{cry}	[MPa]	100.0
λ_{cry}	$[-]$	5.0
k_{cry}	$\left[\frac{\text{W}}{\text{m K}}\right]$	0.235
Δh_{r}	[MPa]	50.0

ACCEPTED MANUSCRIPT

ACCEPTED MANUSCRIPT

SIC is more pronounced. At higher temperatures (above 72°C in this example), SIC is nearly thermally suppressed. Since the maximum degree of crystallinity decreases with increasing temperature, the hysteresis related to SIC reduces as well with increasing temperature, see Fig. 8 b).

A comparison between the experimental results and simulation results shown in Fig. 8 reveals that a good agreement can be observed for the temperature range considered. However, the comparison stimulates also a further detailing of the model approach with respect to a temperature dependency of the parameters λ_{cry} and τ_{l} as discussed in the following.

3.3. Time and temperature dependency of SIC kinetics

For the characterization of the SIC process and its dependencies on time and temperature, the dynamic mechanical testing of rubber specimens at significant large strains is considered, see [13, 38]. The degree of crystallinity decreases with increasing temperature and nearly disappears for high temperatures. In consequence, the stretch required for a significant onset of SIC is shifted to higher stretches in case of higher temperatures. From the experimental measurements, the general relations illustrated in Fig. 2 could be identified. Recently, the SIC kinetics as a function of time have been studied in [13] and [38]. From the experimental data published in [38], the characteristic time τ_{l} as a function of the testing temperature (T) and the applied constant stretch level (λ) could be identified based on the following procedure. For a given initial stretching from the unloaded to the loaded state (λ_{s}) at constant temperature, Eq. (26) results in the characteristic time plot of the degree of crystallinity

$$h(t) = \Phi_{\text{A}} \left[1 - \exp\left(-\frac{t}{\tau} \right) \right] \tag{68}$$

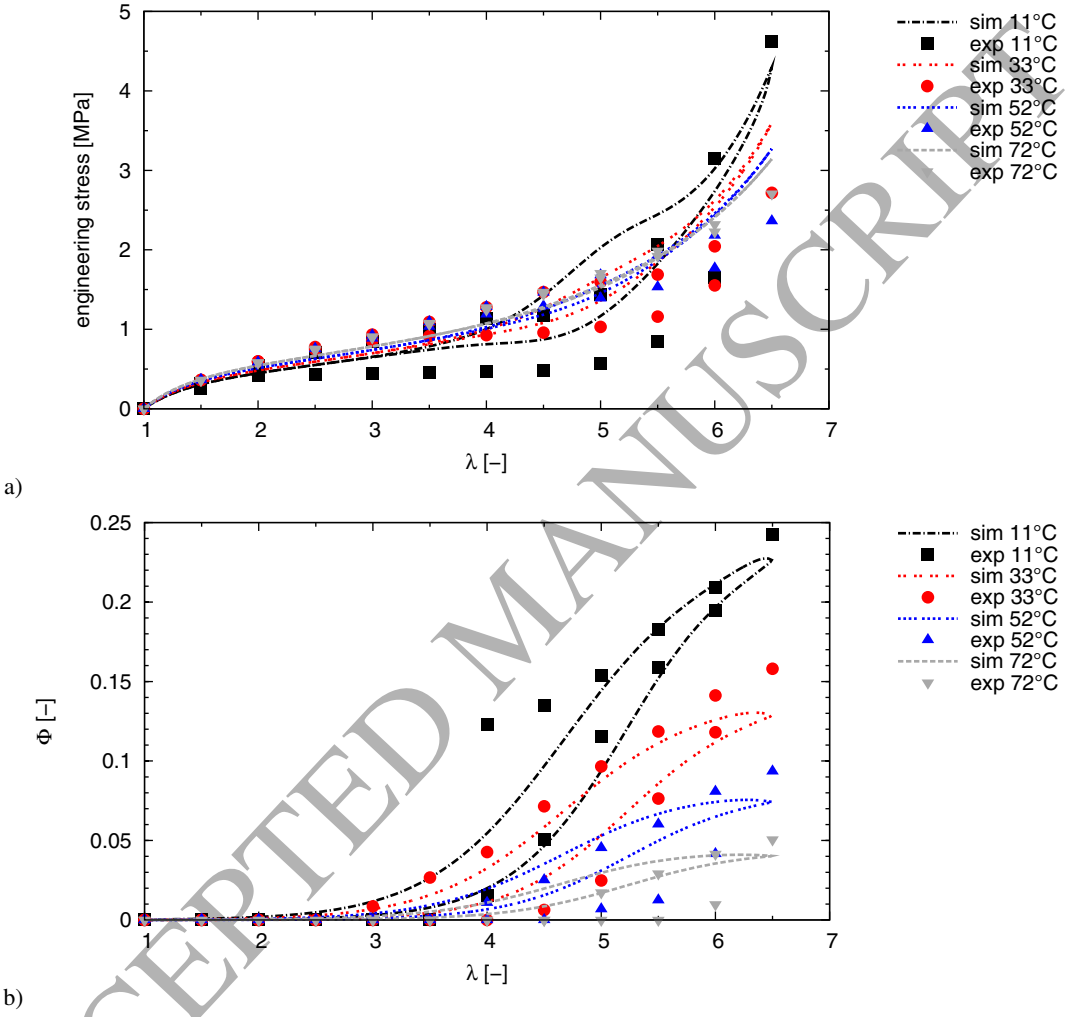

Figure 8: Tensile experiment – loading and unloading (strain rate $1.117 \cdot 10^{-3}$ s^{-1}) at initial temperatures $T = 11°C$, $T = 33°C$, $T = 52°C$ and $T = 72°C$ (experimental data (exp), see [39], and simulation (sim)): a) engineering stress as a function of stretch λ ; b) degree of crystallinity as a function of stretch λ

ACCEPTED MANUSCRIPT

plotted in Fig. 9 for a linear and a logarithmic time scale. $\Phi_{\mathrm{A}} = \Phi^{\infty}(\lambda_{\mathrm{s}}, \Theta)$ denotes the long-term value of the degree of crystallinity for the constant stretch level λ_{s} considered. With the help of the initial slope

$$h'(t=0) = \Phi_{\mathrm{A}} \frac{1}{\tau} = m \quad \rightarrow \quad \tau = \frac{\Phi_{\mathrm{A}}}{m} \tag{69}$$

of the crystallization curve or the determination of the inflection point at $t = \tau$ in the semi-logarithmic plot, the value τ can be identified from the measurement data. In the latter case, the function

$$h(x) = \Phi_{\mathrm{A}} \left[1 - \exp\left(-\frac{10^x}{\tau} \right) \right] \tag{70}$$

is written in terms of the logarithmic time measure x with the relation

$$t = 10^x \, . \tag{71}$$

The second order derivative of $h(x)$ becomes zero at the inflection point, which is determined to

$$h''(x) = 0 \quad \rightarrow \quad x^* = \log(\tau) \tag{72}$$

resulting in

$$t^* = 10^{x^*} = \tau \tag{73}$$

with

$$h(x^*) = \Phi_{\mathrm{A}} \left[1 - \exp(-1) \right] = 0.632 \, \Phi_{\mathrm{A}} \, . \tag{74}$$

In Tab. 3, the crystal growth time τ_{l} is given for different conditions (holding stretch and temperature). The identification is based on data from [38] (Fig. 3) to which the model proposed in Eq. (68) has been applied. The growth time

ACCEPTED MANUSCRIPT

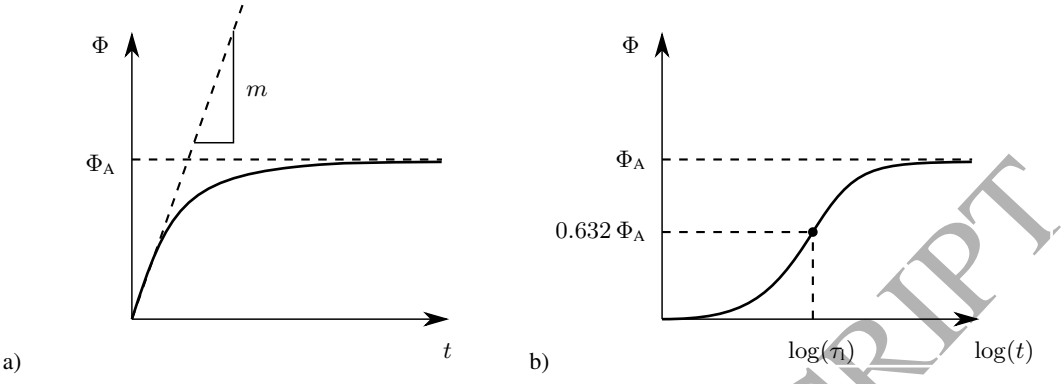

Figure 9: Characteristics of SIC kinetics in terms of the degree of crystallinity Φ as a function of time for a constant stretch level (initial, instantaneous strain step) and constant temperature (m initial slope, Φ_A final long-term value, τ_l model parameter, see Eqs. (37) and (38)): a) degree of crystallinity as a function of time; b) degree of crystallinity as a function of time (logarithmic time scale)

τ_l is determined from the measurement data via the relation stated in Eq. (72) (graphical identification of the inflection point), see also Fig. 9. The modeled evolution of the degree of crystallinity is proportional to the scaling relations proposed in [45] for diffusion-limited reaction kinetics in polymer melts. To take into account the temperature dependency of the crystallization kinetics (see Tab. 3), τ_l can be formulated as a function of temperature $\tau_\mathrm{l}(\Theta)$ in the evolution law of the degree of crystallinity given in Eq. (26), e.g. via an Arrhenius-like approach.

4. Application to steady state rolling tires

As structural example, the proposed model for strain-crystallizing rubber is applied to the analysis of a local material point P in a steady state rolling tire. Due to the rotation of the tire, the material point P undergoes periodic loading at moderate stretches (macroscale). During its service, the temperature of the

ACCEPTED MANUSCRIPT

Table 3: Crystal growth time for Φ_{A}

T [°C]	λ_{A} [−]	τ_{l} [s^{-1}]
−25	4.00	9.047
	4.55	2.833
	5.10	1.650
	5.70	0.852
	6.20	0.367
0	4.00	10.000
	4.55	4.489
	5.10	2.015
	5.70	1.823
25	4.55	10.000
	5.10	3.902
	5.70	1.650
	6.20	1.585
75	5.10	1.650
	5.70	1.650
	6.20	1.650

ACCEPTED MANUSCRIPT

ACCEPTED MANUSCRIPT

material point P is assumed as constant (steady state is reached) and an average temperature of $40°$C is considered, see e.g. a detailed thermo-mechanical study provided in [42]. For a point S located on the mesoscale, a strain amplification is considered, which stems from the presence of a defect or an opening crack as depicted in Fig. 14. First, the macroscopic strain state of point P of the tire cross-section is investigated. From the macroscopic strain field, the strain field at the microscale in the vicinity of a defect is computed. Due to the defect, sufficiently large strains occur in order to observe SIC related processes during steady state rolling of the tire.

For the identification of model parameters of the amorphous phase, it is assumed that no SIC takes place during experimental testing at moderated stretches. The model parameters are chosen in accordance with [35] assuming a purely elastic rubber material at moderate stretches under cyclic loading at a constant temperature of $T = 40°$C. The thermal material properties are selected according to standard values for rubber material from the literature, see e.g. [42]. The model parameters are summarized in Tab. 4.

4.1. Finite element tire model

The FE model of the axisymmetric tire is depicted in Fig. 10. The tire is brought into contact with a rigid plate and loaded by a vertical force of $F_z = 3300$ N. The frictional behavior of the interface wheel-plate is idealized as frictionless, i.e. $\mu = 0$, for the sake of simplicity. The FE segmentation in circumferential direction is depicted in Fig. 11. The cross-section of the tire, its FE discretization and material assignment (rubber material and reinforcement cords) are given in detail in [46] with the difference that the rubber material is represented by the proposed model of this contribution. To compute the periodic

Table 4: Model parameters for amorphous and semi-crystalline phase: steady state rolling tire ($T = 40°\text{C}$)

G_c	[MPa]	0.655
δ	$[-]$	0.09693
G_e	[MPa]	0.751
β	$[-]$	0.2
Θ_0	[K]	313.0
k	$\left[\frac{\text{W}}{\text{m K}}\right]$	0.235
c_0	$\left[\frac{\text{MPa}}{\text{K}}\right]$	1.439
α_V	$\left[\text{K}^{-1}\right]$	0.00048
ρ_0	$\left[\frac{\text{g}}{\text{cm}^3}\right]$	1.10
G_{cry}	[MPa]	0.0005
τ_{l}	[s]	1.65; 0.05
τ_{unl}	[s]	0.001 τ_{l}
A	$\left[\text{mm}^2\right]$	1.0
Θ_{R}	[K]	155.0
b	$[-]$	0.005
E_{cry}	[MPa]	100.0
λ_{cry}	$[-]$	4.5
k_{cry}	$\left[\frac{\text{W}}{\text{m K}}\right]$	0.235
Δh_{r}	[MPa]	50.0

ACCEPTED MANUSCRIPT

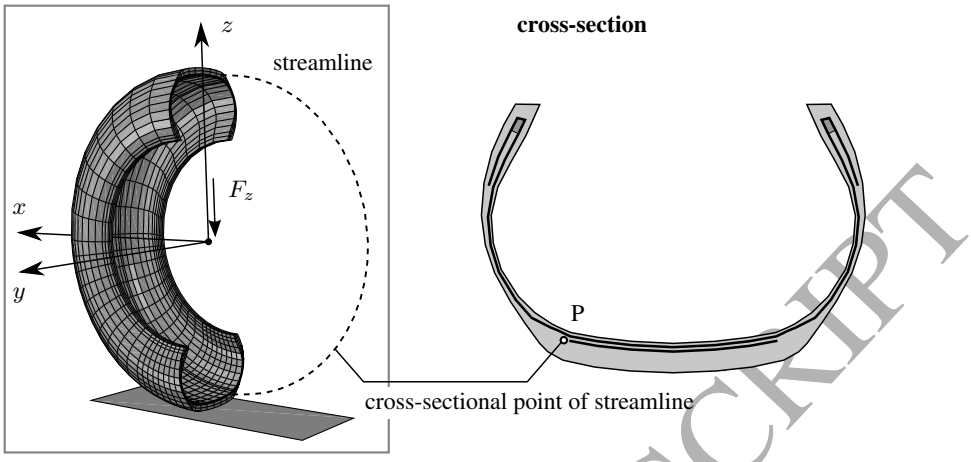

Figure 10: FE tire model and streamline of cross-sectional point P near tread belt

deformation history of point P, load case A (inner pressure $p = 1.70$ bar, translational velocity $v = 80$ km/h, vertical force $F_z = 3300$ N, see [46]) is considered in the following.

In Fig. 12, the deformation history of point P is depicted in terms of the components of $\mathbf{F}$ as a function of the circumferential angle φ represented in the local (rotated) coordinate system by following the streamline associated to point P.

From the components F_{ij}, the principal stretches and the associated principal stretch directions $\mathbf{n}_1$, $\mathbf{n}_2$ and $\mathbf{n}_3$ are computed for each circumferential angle. The result is plotted in terms of the three principle stretches $\lambda_{\text{macro},1}$, $\lambda_{\text{macro},2}$ and $\lambda_{\text{macro},3}$ (macroscale) in Fig. 13.

4.2. Strain-induced crystallization representation

From the computed macroscopic deformation signal in terms of $\mathbf{F}$, a microscopic deformation field in terms of principal stretches has been computed at the meso-/microscale for point S located near an assumed material singularity (crack). In Fig. 14, the macro-meso-micro-transition is illustrated. The micro-

ACCEPTED MANUSCRIPT

ACCEPTED MANUSCRIPT

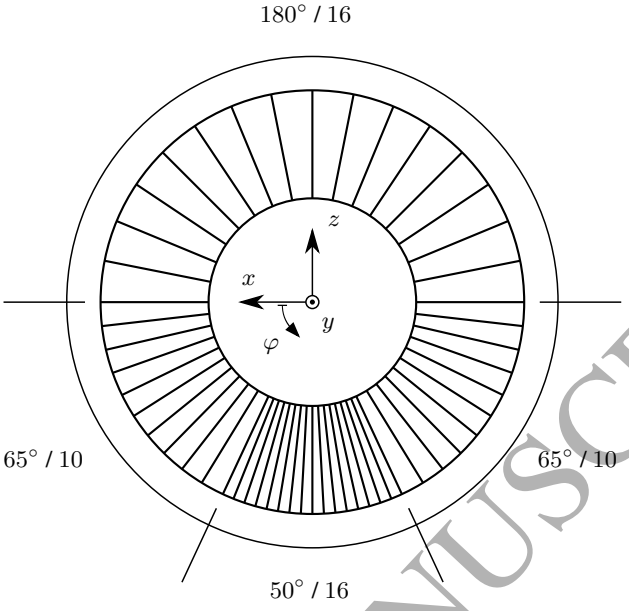

Figure 11: Circumferential FE discretization (segmentation) of the FE tire model

scopic stretch field is computed assuming a strain amplification of the macroscopic strain field by the amplification factor S_{P} in principal stretch directions (affine micro-macro deformation in terms of the stretch directions of point P and S). The opening of the crack tip at point S induces a scaling of the strain field of point P to significantly large strains at which SIC-related phenomena are expected. Note that for the quantitative computation of the strain field at the crack tip, advanced numerical methods can be used, see e.g. [47], which is out of the scope of the present contribution. In a simplified form, the principal stretches at the microscale become

$$\lambda_1 = \frac{1}{\sqrt{S_{\mathrm{P}}}}\,\lambda_{\text{macro},1}\,, \quad \lambda_2 = S_{\mathrm{P}}\,\lambda_{\text{macro},2}\,, \quad \lambda_3 = \frac{1}{\sqrt{S_{\mathrm{P}}}}\,\lambda_{\text{macro},3}\,, \tag{75}$$

with the same volume change $J = \frac{1}{\sqrt{S_{\mathrm{P}}}}\,\lambda_{\text{macro},1}\,S_{\mathrm{P}}\,\lambda_{\text{macro},2}\,\frac{1}{\sqrt{S_{\mathrm{P}}}}\,\lambda_{\text{macro},3} = \lambda_1\,\lambda_2\,\lambda_3 = J$. To relate the strain amplification factor S_{P} to the initial crack width Δ of a defect in the mesostructure, a mesostructure with a unit length of

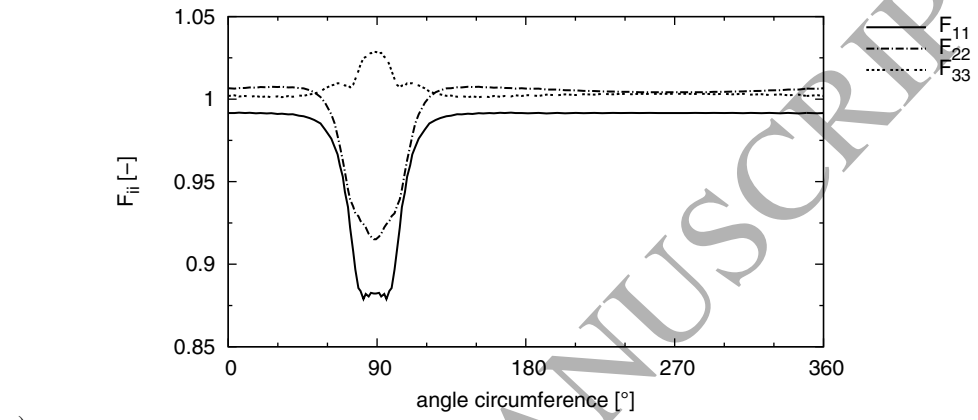

a)

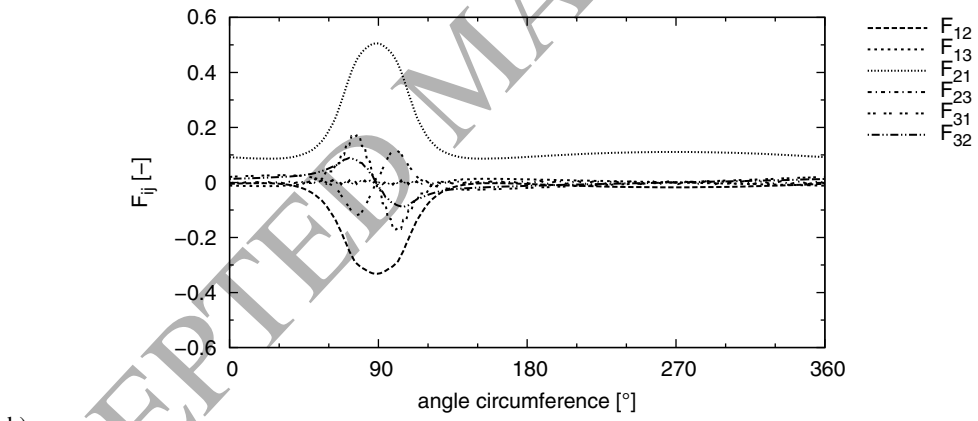

b)

Figure 12: Point P: components F_{ij} of the deformation gradient $\mathbf{F}$ as a function of the circumferential angle φ, see Fig. 11: a) components F_{ii}; b) components F_{ij}

ACCEPTED MANUSCRIPT

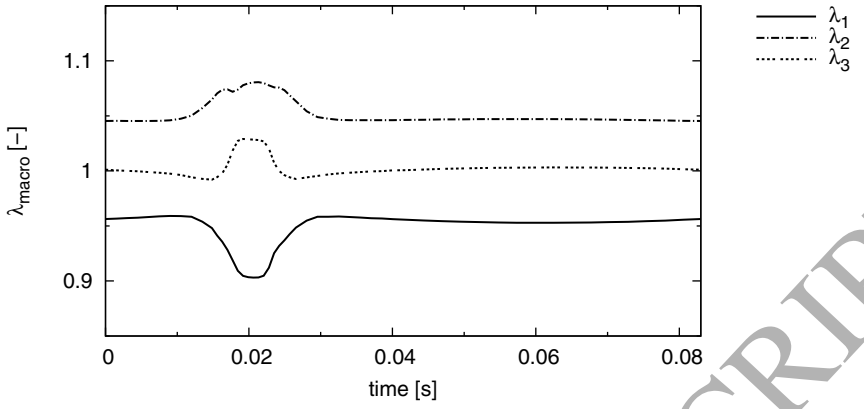

Figure 13: Point P: principal stretches $\lambda_{\text{macro},1}$, $\lambda_{\text{macro},2}$ and $\lambda_{\text{macro},3}$ (macroscale) in $\mathbf{n}_1$, $\mathbf{n}_2$ and $\mathbf{n}_3$ direction, respectively, as a function of time for one cycle duration $T = 0.083$ s (rotational velocity $\Omega = 75.673$ s^{-1} of the tire)

1 is considered as illustrated in Fig. 14. The dimensionless width of the unloaded crack is termed Δ. The unit cube on the mesoscale is deformed by the macroscopic stretch λ_{macro} (boundary conditions). As limit case, parts of the mesostructure with the total length of $(1 - \Delta)$ will not deform, while parts with length Δ located at the vicinity of the crack will deform with the stretch $\lambda_{\text{macro}}\, S_{\text{P}}$. In consequence, the relation

$$\lambda_{\text{macro}} \cdot 1 = 1 \cdot (1 - \Delta) + S_{\text{P}}\, \lambda_{\text{macro}}\, \Delta \tag{76}$$

describes the overall stretch of the mesostructure consisting of nearly unstretched parts $(1 - \Delta)$ with stretch ≈ 1 and the part Δ with stretch $S_{\text{P}}\, \lambda_{\text{macro}}$. Hence, the strain amplification factor in tensile direction is related to the initial width Δ of the undeformed crack via the condition

$$\Delta < \frac{\lambda_{\text{macro}} - 1}{\lambda_{\text{macro}}\, S_{\text{P}} - 1}\,, \tag{77}$$

as illustrated in Fig. 14. In summary, the assumption used for the macro-to-micro transition is based on a time-, temperature- and deformation-constant amplifica-

ACCEPTED MANUSCRIPT

ACCEPTED MANUSCRIPT

tion factor S_{P}, which scales the macroscopic principal stretches to the microscopical counterparts. Here again, only a scaling is considered and, in consequence, also the principal stretch directions are considered to be the same at the macroscale and mesoscale. Obviously, this is a strong simplification since both, the principal stretches as well as the principal stretch directions will vary as a function of the crack geometry and the current state of the point at the macroscale. If a specific problem is investigated, a homogenization method has to be employed which provides the two-way-coupling of macro- and mesoscale without the simplified assumption of a strain amplification factor.

The result of the stretch amplification at the microscale is plotted in Fig. 15 and is used as input signal for the computation of the material response at the microscale in the following. The engineering stress-stretch response, the degree of crystallinity as well as the temperature variation at the microscale have been computed considering SIC for the present example. In Fig. 16, the computed results for five consecutive cycles (rotations of the tire) from the beginning $t = 0$ s are provided (time step $\Delta t = 0.000005$ s). The material response has been computed considering two examples of different time-dependent SIC effects (example 1: $\tau_{\mathrm{l}} = 1.65$ s – value identified from experiment; example 2: $\tau_{\mathrm{l}} = 0.05$ s – value for comparison). In Fig. 16, it can be seen that SIC leads to a stress increase upon stretching. Since the characteristic time $\tau_{\mathrm{l}} = 1.65$ s for crystal growth is relatively large compared to the loading time within the tire, e.g. in terms of the cycle duration $T = 0.083$ s, the degree of crystallinity only shows a small increase upon loading of the specimen and reaches a steady state after several cycles, see Fig. 16 b). For the characteristic time $\tau_{\mathrm{l}} = 0.05$ s, the evolution of the degree of crystallinity is more pronounced (faster growth kinetics in case of example 2). From the relatively negligible variation of the degree of

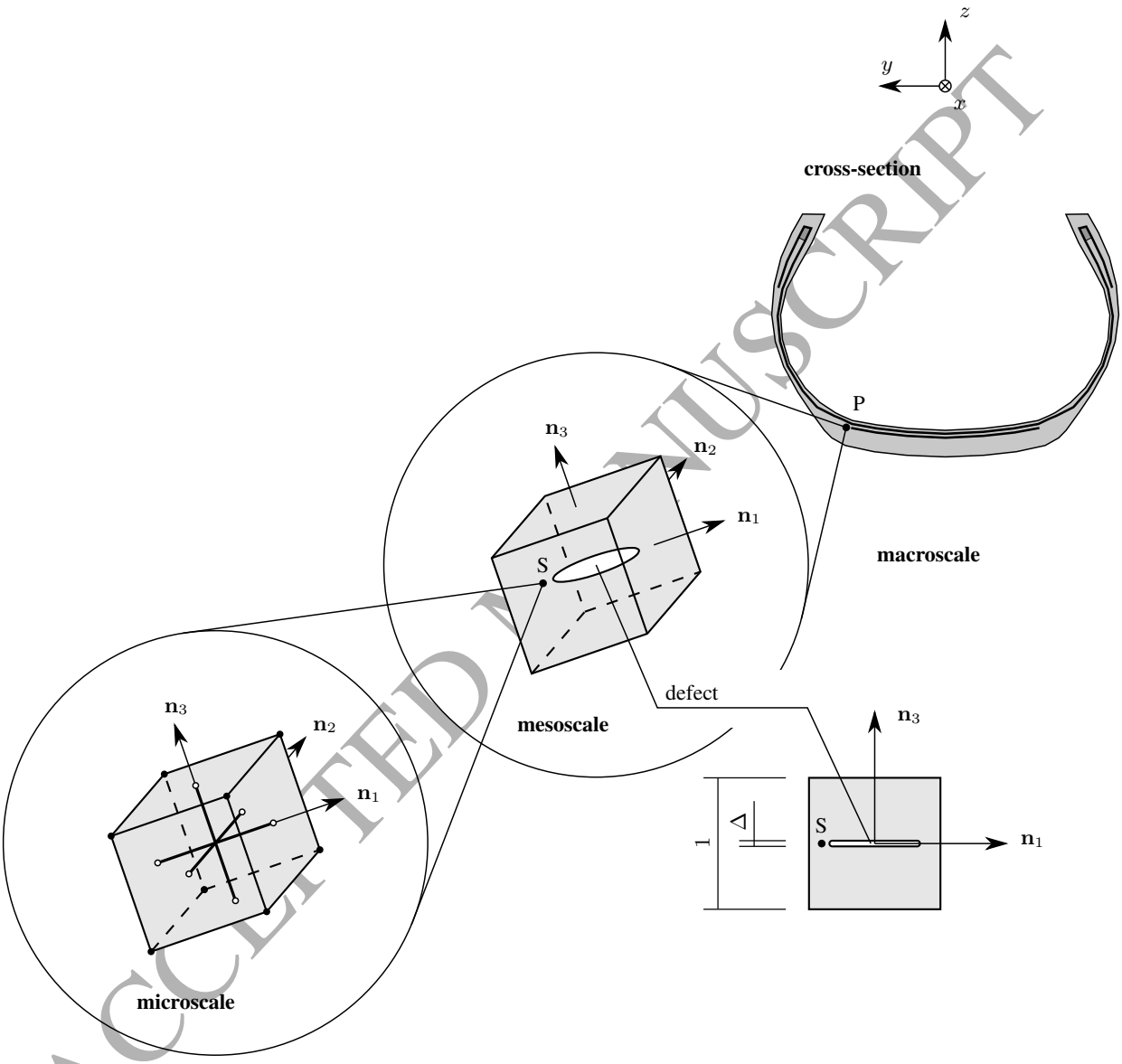

Figure 14: Macro-meso-micro transition for point P in the tire with a defect on the mesoscale and the strain state of a point S in the vicinity of the defect on the microscale

ACCEPTED MANUSCRIPT

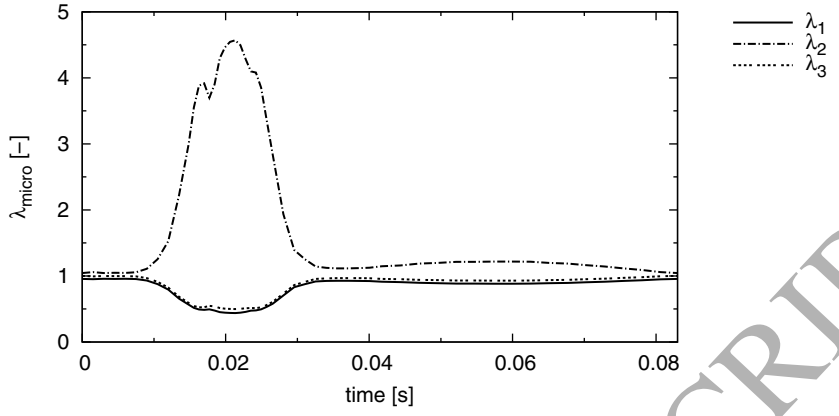

Figure 15: Point S: principal stretches λ_1, λ_2 and λ_3 in $\mathbf{n}_1$, $\mathbf{n}_2$ and $\mathbf{n}_3$ direction, respectively, as a function of time for one cycle duration $T = 0.083$ s (rotational velocity $\Omega = 75.673$ s^{-1} of the tire)

crystallinity with elapsing time, it can be explained that the SIC process in case of $\tau_{\mathrm{l}} = 1.65$ s is not of pronounced dissipative nature. If the characteristic time τ_{l} is smaller (see example 2 with $\tau_{\mathrm{l}} = 0.05$ s), the temperature plot in Fig. 16 c) shows a significant increase of the average temperature of the material point considered due to the more pronounced contribution of SIC effects to the dissipative heating of the material. For larger characteristic growth times τ_{l}, nearly no SIC hystereses will appear since the growth kinetics of SIC are not fast enough for the loading considered. Furthermore, the value of the degree of crystallinity is small in this example (less than 1.5%). In consequence, the temperature peaks visible for both cases in Fig. 16 c) are mainly related to the thermo-elastic coupling of the amorphous phase.

Details to incorporate an evolving temperature field within a steady state FE tire simulation are provided in [42].

The pull back projection of the material response of the microscale to the Cartesian frame on the macroscale is not considered in this contribution and, in

ACCEPTED MANUSCRIPT

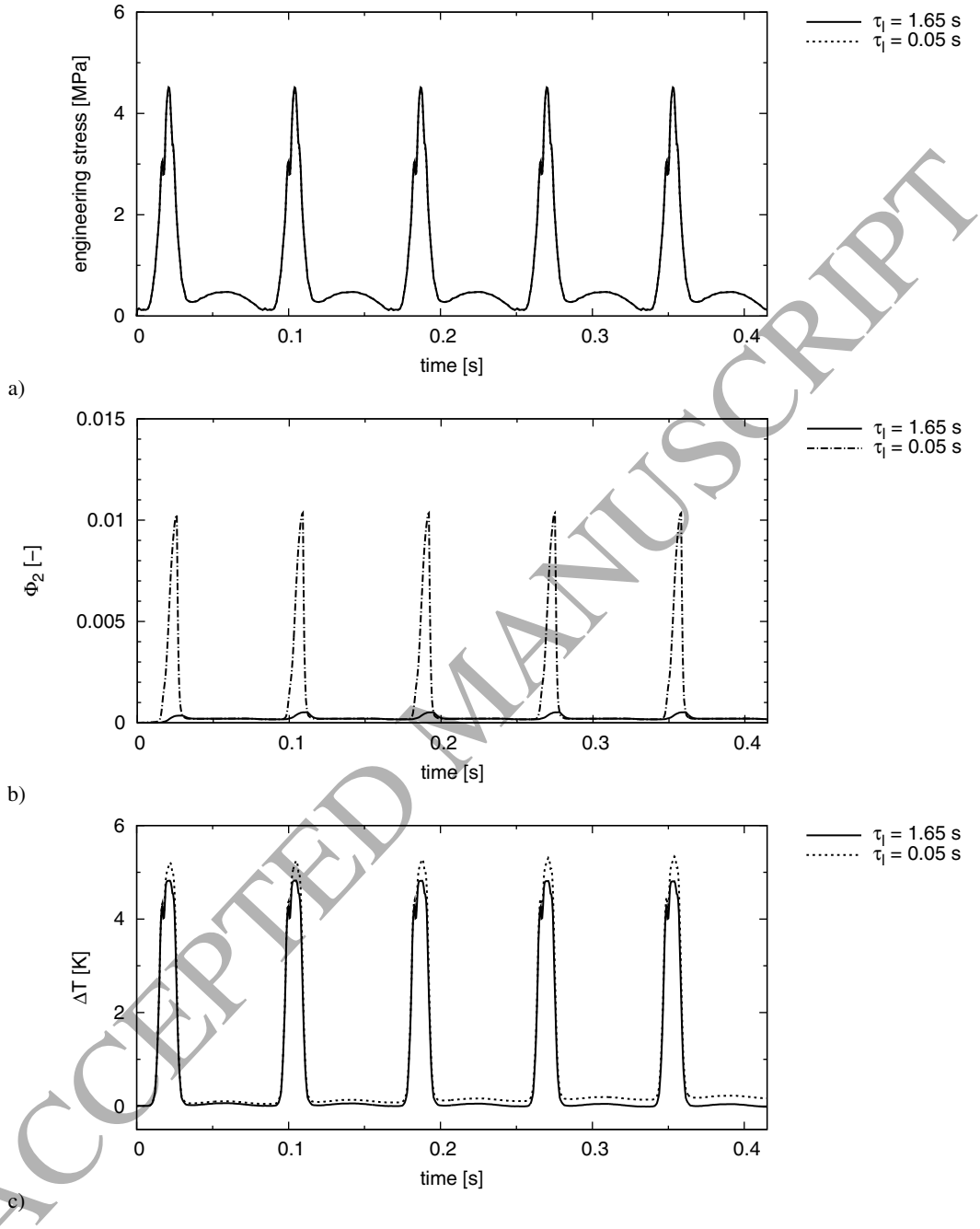

Figure 16: Periodic state of the material point S on the mesoscale including SIC phenomena, plotted for five cycles ($T = 0.083$ s) after start of rolling ($t = 0$ s) in $\mathbf{n}_2$ direction for two characteristic growth times τ_l: a) engineering stress as a function of time; b) degree of crystallinity as a function of time; c) temperature variation as a function of time

ACCEPTED MANUSCRIPT

ACCEPTED MANUSCRIPT

consequence, no interaction with the macroscale is computed so far. A full two-scale simulation can be accomplished in two ways. First, an analytical micro-to-macro transition can be established based on the microscale model and the homogeneous macroscopic field, see e.g. [48, 49, 50]. Second, in case of a heterogeneous mesoscale, numerical homogenization techniques have to be involved, e.g. as discussed in [51].

To further characterize the material response of the semi-crystalline phase, the degree of crystallinity can be used as a measurable indicator from experiments to link the observed structural response to the material properties of the material (amorphous and semi-crystalline phase). Therefore, relations between the stress-strain response at large stretches and the degree of crystallinity have to be revealed by further experiments.

5. Discussion

In the past, various experimental studies on SIC in crystallizing rubber revealed the variety of phenomena related to SIC. These observations stimulated the development of phenomenological and physically based models for SIC to take into account these effects on the material scale (material behavior) and on the structural scale (resulting consequences on the structural level, e.g. crack growth resistance, induced anisotropy) within numerical simulations.

Since SIC is linked to a directional material behavior (strain-induced origin) and, in consequence, depends on the direction considered, 1D material models are often developed to track this direction-specific behavior to numerically represent the complex constitutive behavior. In the past, model developments for SIC used the phase field approach, e.g. [21, 22], the elastoplastic framework with a critical stretch level (time-independent), e.g. [29, 30], and the concept of

ACCEPTED MANUSCRIPT

ACCEPTED MANUSCRIPT

viscoelasticity (time-dependent), e.g. [27, 28], or mixtures of both. In reality, time-independent as well as time-dependent SIC kinetics are likely to occur in a superposed manner. Furthermore, SIC kinetics depend on temperature and strain states observed (history-dependent), e.g. [52, 53, 32, 31].

For investigations on the structural scale, the models for SIC have to be implemented into numerical methods allowing the solution of boundary value problems (strong or weak forms) involving displacement, temperature and other significant solution fields of external state variables. Commonly, the 1D models for SIC are transferred to a 3D constitutive law by the concept of representative directions [54, 55]. In this case, the material response and associated quantities [56] are projected to a 3D setting using different representative geometries (representative volumes) and an analytical expression for the 1D to 3D transition. The micro-sphere approach [49] is similar to the concept of representative directions, but mainly focuses on averaging the free energies of single polymer chains (microscale) over different space orientations of the micro-sphere (representative directions) to obtain the total free energy (macroscale) in terms of continuum mechanical deformation or strain tensors. The micro-sphere approach has been further developed to also take into account inelastic material behavior [50] and has also been used to generalize SIC effects for a 3D setting, e.g. [25, 26].

The concept used in this work is based on a unit cube with varying directional reinforcement axes (current principal stretch directions) instead of a sphere (geometry). Orthotropic material laws with time-independent, fixed material axes can be seen as another special case. Furthermore, one has to distinguish if only the SIC effects (crystalline or semi-crystalline phase) is represented by the concept of representative directions or if the combination of amorphous and crystalline parts is addressed.

ACCEPTED MANUSCRIPT

Among the models for SIC proposed in the literature, a model for SIC accounting for coupling effects between displacement and temperature field is not standard so far. This work makes an attempt to contribute to the investigation of SIC effects on the structural scale by mainly focusing on adequate finite element implementations of the model approach proposed. The model approach is mainly based on a phenomenological ansatz in combination with physically motivated evolution laws for the evolution of the degree of crystallinity upon loading and unloading. Furthermore, the model is characterized by a small number of unknowns, which can be identified from standard experiments (WAXD, tensile tests etc.) since the model directly incorporates the phenomena observed during standard experiments. It has to be pointed out that other, more sophisticated, models for SIC exist in the literature, which allow to explain the phenomena observed with the help of physical and chemical theories, especially representing phase changes, crystallinity-dependent heat capacity etc. Nevertheless, these models often use a large number of model parameters and operate on the material scale, i.e. they have not been used within finite element analyses. In consequence, a link of SIC phenomena to the structural scale, e.g. evolution of SIC for cyclic loading state, has been established in this work. Other constitutive models can be employed in the same framework. It has to be mentioned that experimental validation on structural scale (e.g. tire) is hard to accomplish and might concentrate on the consequences of SIC (crack growth resistance, extended lifetime).

6. Conclusion

In this contribution, temperature-dependent SIC is modeled at the microscale via an FE representation consisting of an amorphous rubber phase and a unidirectional reinforcement (semi-crystalline phase) in the principal strain directions

ACCEPTED MANUSCRIPT

ACCEPTED MANUSCRIPT

of the strain field. The model uses an FE unit cube with rebar reinforcements as RVE. The temperature field is taken into account and the representation of temperature- and time-dependent SIC kinetics is addressed. SIC phenomena are computed in the principal directions of the strain field. Induced anisotropy effects in the material's mechanical and thermal response are captured by the unidirectional reinforcement. A micro-meso-macro transition is considered via the strain field and a strain amplification to form a link between the structural response of a steady state rolling tire and the material response at the microscale with SIC phenomena.

Appendix A. Derivations

The linearized terms of Eq. (54) are given in the following:

Temperature of a point of the rebar

The temperature at a given point of the rebar is expressed with the help of its nodal temperatures and linear shape functions,

$$\Theta = \mathbf{N}(\xi)\,\boldsymbol{\Theta}^e, \tag{A.1}$$

where

$$\mathbf{N}(\xi) = \left[-\tfrac{1}{2}(\xi - 1) \quad \tfrac{1}{2}(\xi + 1) \right] \tag{A.2}$$

holds and

$$\boldsymbol{\Theta}^e = \begin{bmatrix} \Theta_1 \\ \Theta_2 \end{bmatrix} \tag{A.3}$$

is the vector of nodal temperature values. The temperature gradient is then

$$\nabla_{\mathbf{X}}(\Theta) = \frac{1}{L} \begin{bmatrix} -1 & 1 \end{bmatrix} \begin{bmatrix} \Theta_1 \\ \Theta_2 \end{bmatrix}. \tag{A.4}$$

At the integration point $\xi = 0$, the temperature is computed as

$$\Theta_m = \frac{\Theta_1 + \Theta_2}{2} \,. \tag{A.5}$$

Linearized weak form of the balance of momentum

The derivation of the scalar Green-Lagrange strain E_s with respect to the nodal displacement values $u_{i,1}$ at the rebar nodes is

$$\frac{\partial E_\mathrm{s}}{\partial u_{i,1}} = \frac{\partial E_\mathrm{s}}{\partial \lambda_\mathrm{s}} \frac{\partial \lambda_\mathrm{s}}{\partial l} \frac{\partial l}{\partial u_{i,1}} \,. \tag{A.6}$$

The partial derivatives are

$$\frac{\partial E_\mathrm{s}}{\partial \lambda_\mathrm{s}} = \lambda_\mathrm{s} \,, \quad \frac{\partial \lambda_\mathrm{s}}{\partial l} = \frac{1}{L} \,. \tag{A.7}$$

The partial derivative of the current length l with respect to the nodal displacements of the rebar is

$$\frac{\partial l}{\partial u_{i,1}} = -\frac{1}{l} \left[(X_{i,2} + u_{i,2}) - (X_{i,1} + u_{i,1}) \right] . \tag{A.8}$$

The variation of the Green-Lagrange strain results in

$$\delta E_\mathrm{s} = \sum_{i=1}^{3} \frac{\partial E_\mathrm{s}}{\partial u_{i,1}} \delta u_{i,1} + \sum_{i=1}^{3} \frac{\partial E_\mathrm{s}}{\partial u_{i,2}} \delta u_{i,2}. \tag{A.9}$$

The linearized form of the balance of momentum is

$$\left. \frac{\partial G_m^e}{\partial \mathbf{u}} \right|_p \Delta \mathbf{u}^e = \int_{(s)} \delta E_\mathrm{s} \, \Delta S_\mathrm{cry} \, A \, \mathrm{d}s + \int_{(s)} \delta \Delta E_\mathrm{s} \, S_\mathrm{cry} \, A \, \mathrm{d}s \,. \tag{A.10}$$

The linearization of E_s yields

$$\Delta E_\mathrm{s} = \frac{1}{L^2} \begin{bmatrix} -(X_{i,2} - X_{i,1}) - (u_{i,2} - u_{i,1}) & (X_{i,2} - X_{i,1}) + (u_{i,2} - u_{i,1}) \end{bmatrix} \begin{bmatrix} \Delta u_{i,1} \\ \Delta u_{i,2} \end{bmatrix} \tag{A.11}$$

ACCEPTED MANUSCRIPT

ACCEPTED MANUSCRIPT

and the variation of the linearization results in

$$\Delta\delta E_{\mathrm{s}} = \frac{1}{L^2}\left(\begin{bmatrix} \delta u_{i,1} & \delta u_{i,2} \end{bmatrix}\begin{bmatrix} 1 & -1 \\ -1 & 1 \end{bmatrix}\begin{bmatrix} \Delta u_{i,1} \\ \Delta u_{i,2} \end{bmatrix}\right) \tag{A.12}$$

as a function of the nodal displacements of the rebar. The first integral in Eq. (A.10) is evaluated with the help of the stress relation $\Delta S_{\mathrm{cry}} = C_{\mathrm{cry}}\,\Delta E_{\mathrm{s}}$ linearized with respect to the nodal displacements,

$$\begin{aligned}\int_{(s)} \delta E_{\mathrm{s}}\,\Delta S_{\mathrm{cry}}\,A\,\mathrm{d}s &= \int_{(s)} \begin{bmatrix} \delta u_{i,1} & \delta u_{i,2} \end{bmatrix}\frac{A\,C_{\mathrm{cry}}}{L^4}\begin{bmatrix} -\Delta X_i + u_{i,1} - u_{i,2} \\ \Delta X_i - u_{i,1} + u_{i,2} \end{bmatrix} \\ &\qquad \begin{bmatrix} -\Delta X_j + u_{j,1} - u_{j,2} \\ \Delta X_j - u_{j,1} + u_{j,2} \end{bmatrix}^{\mathrm{T}}\begin{bmatrix} \Delta u_{i,1} \\ \Delta u_{i,2} \end{bmatrix}\mathrm{d}s \\ &= \begin{bmatrix} \delta u_{i,1} & \delta u_{i,2} \end{bmatrix}\frac{A\,C_{\mathrm{cry}}}{L^3}\begin{bmatrix} k_{ij} & -k_{ij} \\ -k_{ij} & k_{ij} \end{bmatrix}\begin{bmatrix} \Delta u_{i,1} \\ \Delta u_{i,2} \end{bmatrix}\end{aligned} \tag{A.13}$$

with

$$\begin{aligned} k_{ij} &= (\Delta X_i + \Delta u_i)\,(\Delta X_j + \Delta u_j) \\ &= \Delta X_i\,\Delta X_j + \Delta u_i\,\Delta X_j + \Delta X_i\,\Delta u_j + \Delta u_i\,\Delta u_j\,. \end{aligned} \tag{A.14}$$

The second integral in Eq. (A.10) results in

$$\begin{aligned}\int_{(s)} \delta\Delta E_{\mathrm{s}}\,S_{\mathrm{cry}}\,A\,\mathrm{d}s &= \int_{(s)} \frac{1}{L^2}\left(\begin{bmatrix} \delta u_{i,1} & \delta u_{i,2} \end{bmatrix}\begin{bmatrix} 1 & -1 \\ -1 & 1 \end{bmatrix}\begin{bmatrix} \Delta u_{i,1} \\ \Delta u_{i,2} \end{bmatrix}\right) \\ &\qquad S_{\mathrm{cry}}\,A\,\mathrm{d}s \\ &= \begin{bmatrix} \delta u_{i,1} & \delta u_{i,2} \end{bmatrix}\frac{S_{\mathrm{cry}}\,A}{L}\begin{bmatrix} 1 & -1 \\ -1 & 1 \end{bmatrix}\begin{bmatrix} \Delta u_{i,1} \\ \Delta u_{i,2} \end{bmatrix}.\end{aligned} \tag{A.15}$$

ACCEPTED MANUSCRIPT

From these intermediate results, the matrices

$$\mathbf{A}_1 = \frac{C_{\text{cry}}\, A}{L^3} \begin{bmatrix} k_{11} & k_{12} & k_{13} \\ k_{21} & k_{22} & k_{23} \\ k_{31} & k_{32} & k_{33} \end{bmatrix}, \quad \mathbf{A}_2 = \frac{S_{\text{cry}}\, A}{L} \begin{bmatrix} 1 & 0 & 0 \\ 0 & 1 & 0 \\ 0 & 0 & 1 \end{bmatrix} \tag{A.16}$$

and the residual vector

$$\mathbf{r}_1 = \frac{S_{\text{cry}}\, A}{L} \begin{bmatrix} \Delta X_1 + \Delta u_1 \\ \Delta X_2 + \Delta u_2 \\ \Delta X_3 + \Delta u_3 \\ -\Delta X_1 - \Delta u_1 \\ -\Delta X_2 - \Delta u_2 \\ -\Delta X_3 - \Delta u_3 \end{bmatrix}, \tag{A.17}$$

can be found, see Eq. (55). The linearization of the weak form of the balance of momentum with respect to temperature is defined as

$$\left.\frac{\partial G_m^e}{\partial \boldsymbol{\Theta}}\right|_p \Delta\boldsymbol{\Theta}^e = \int_{(s)} \delta E_{\text{s}}\, \Delta S_{\text{cry}}\, A \, \mathrm{d}s \,. \tag{A.18}$$

With the term

$$\Delta S_{\text{cry}} = \frac{\partial S_{\text{cry}}}{\partial \boldsymbol{\Theta}}\, \Delta\boldsymbol{\Theta}^e \,, \tag{A.19}$$

ACCEPTED MANUSCRIPT

Eq. (A.18) becomes

$$\int_{(s)} \delta E_{\mathrm{s}}\, \Delta S_{\mathrm{cry}}\, A\, \mathrm{d}s = \left[\begin{array}{cc} \delta u_{i,1} & \delta u_{i,2} \end{array}\right] \left[\begin{array}{c} -\Delta X_1 - \Delta u_1 \\ -\Delta X_2 - \Delta u_2 \\ -\Delta X_3 - \Delta u_3 \\ \Delta X_1 + \Delta u_1 \\ \Delta X_2 + \Delta u_2 \\ \Delta X_3 + \Delta u_3 \end{array}\right] \frac{A}{2\,L}\, \left.\frac{\partial S_{\mathrm{cry}}}{\partial \Theta}\right|_{\Theta_m} \left[\begin{array}{cc} 1 & 1 \end{array}\right] \left[\begin{array}{c} \Delta\Theta_1 \\ \Delta\Theta_2 \end{array}\right]. \tag{A.20}$$

From Eq. (A.20), a tangent term can be identified,

$$\left.\frac{\partial G_m^e}{\partial \boldsymbol{\Theta}}\right|_p = \left[\begin{array}{cc} \delta u_{i,1} & \delta u_{i,2} \end{array}\right] \left[\begin{array}{cc} -\mathbf{C}_1 & -\mathbf{C}_1 \\ \mathbf{C}_1 & \mathbf{C}_1 \end{array}\right], \tag{A.21}$$

with

$$\mathbf{C}_1 = \frac{A}{2\,L}\, \left.\frac{\partial S_{\mathrm{cry}}}{\partial \Theta}\right|_{\Theta_m} \left[\begin{array}{c} \Delta X_1 + \Delta u_1 \\ \Delta X_2 + \Delta u_2 \\ \Delta X_3 + \Delta u_3 \end{array}\right]. \tag{A.22}$$

Linearized weak form of the balance of energy

The linearization with respect to the displacements is given by

$$\left.\frac{\partial G_t^e}{\partial \mathbf{u}}\right|_p \Delta\mathbf{u} = \int_{(s)} \Delta Q\, \nabla_{\mathbf{X}}\left(\delta\Theta\right) A\, \mathrm{d}s + \int_{(s)} \left(\Delta w_{\mathrm{cry}} - \Delta c_{\mathrm{cry}}\, \dot{\Theta}\right) \delta\Theta\, A\, \mathrm{d}s \tag{A.23}$$

and contains parts stemming from the heat flux, the heat capacity and the work contribution. The first term can be evaluated with the help of the chain rule,

$$\Delta Q = \frac{\partial Q}{\partial \mathbf{u}}\, \Delta\mathbf{u}^e = \frac{\partial Q}{\partial \lambda_{\mathrm{s}}}\, \frac{\partial \lambda_{\mathrm{s}}}{\partial l}\, \frac{\partial l}{\partial \mathbf{u}}\, \Delta\mathbf{u}^e, \tag{A.24}$$

ACCEPTED MANUSCRIPT

using the constitutive heat flux law

$$\frac{\partial Q}{\partial \lambda_\mathrm{s}} = \frac{2\,k_\mathrm{cry}}{\lambda_\mathrm{s}^3}\,\nabla_\mathbf{X}\left(\Theta\right). \tag{A.25}$$

The derivative of Q results in

$$\frac{\partial Q}{\partial \mathbf{u}} = \frac{2\,k_\mathrm{cry}}{\lambda_\mathrm{s}^4\,L^2}\left[\begin{array}{cc} -\Delta X_i - \Delta u_i & \Delta X_i + \Delta u_i \end{array}\right]. \tag{A.26}$$

If the integration is carried out, one obtains

$$\left.\frac{\partial G_t^e}{\partial \mathbf{u}}\right|_p \Delta\mathbf{u}^e = \int_{(s)} \Delta Q\,\nabla_\mathbf{X}\left(\delta\Theta\right) A\,\mathrm{d}s = \left[\begin{array}{cc} \delta\Theta_1 & \delta\Theta_2 \end{array}\right] \frac{2\,A\,k_\mathrm{cry}}{\lambda_\mathrm{s}^4 L^3}\left(\Theta_2 - \Theta_1\right) \left[\begin{array}{cc} \Delta X_i + \Delta u_i & -\Delta X_i - \Delta u_i \\ -\Delta X_i - \Delta u_i & \Delta X_i + \Delta u_i \end{array}\right] \left[\begin{array}{c} \Delta u_{i,1} \\ \Delta u_{i,2} \end{array}\right] \tag{A.27}$$

with the tangent term

$$\left.\frac{\partial G_t^e}{\partial \mathbf{u}}\right|_p = \left[\begin{array}{cc} \delta\Theta_1 & \delta\Theta_2 \end{array}\right] \left[\begin{array}{cc} \mathbf{D}_1 & -\mathbf{D}_1 \\ -\mathbf{D}_1 & \mathbf{D}_1 \end{array}\right] \tag{A.28}$$

and the components

$$\mathbf{D}_1 = \frac{2\,A\,k_\mathrm{cry}}{\lambda_\mathrm{s}^4\,L^3}\left(\Theta_2 - \Theta_1\right)\left[\begin{array}{ccc} \Delta X_1 + \Delta u_1 & \Delta X_2 + \Delta u_2 & \Delta X_3 + \Delta u_3 \end{array}\right]. \tag{A.29}$$

Integration of the second term in Eq. (A.23) (work contribution and heat capacity),

$$\Delta w_\mathrm{cry} - \Delta c_\mathrm{cry}\,\dot{\Theta} = \left[\frac{\partial w_\mathrm{int}}{\partial E_\mathrm{s}} + \frac{\partial w_\mathrm{ext}}{\partial E_\mathrm{s}} - \frac{\partial c_\mathrm{cry}}{\partial E_\mathrm{s}}\,\dot{\Theta}\right]\frac{\partial E_\mathrm{s}}{\partial u_i}\,\Delta u_i\,, \tag{A.30}$$

results in

$$\int_{(s)} \left(\Delta w_\mathrm{cry} - \Delta c_\mathrm{cry}\,\dot{\Theta}\right)\,\delta\Theta\,A\,\mathrm{d}s = \left[\begin{array}{cc} \delta\Theta_1 & \delta\Theta_2 \end{array}\right] \left[\begin{array}{cc} -\mathbf{D}_2 & \mathbf{D}_2 \\ -\mathbf{D}_2 & \mathbf{D}_2 \end{array}\right] \left[\begin{array}{c} \Delta u_{i,1} \\ \Delta u_{i,2} \end{array}\right] \tag{A.31}$$

ACCEPTED MANUSCRIPT

with

$$\begin{aligned}\mathbf{D}_2 = \frac{A}{2\,L}\Bigg\{ & -\left(\frac{\partial^2 \Psi_{\text{cry}}}{\partial \Phi\, \partial E_{\text{s}}} - \Theta\, \frac{\partial^3\, \Psi_{\text{cry}}}{\partial \Theta\, \partial \Phi\, \partial E_{\text{s}}}\right) \dot{\Phi} \\ & - \left(\frac{\partial \Psi_{\text{cry}}}{\partial \Phi} - \Theta\, \frac{\partial^2 \Psi_{\text{cry}}}{\partial \Theta\, \partial \Phi}\right) \frac{\partial \dot{\Phi}}{\partial E_{\text{s}}} \\ & + \Theta\, \frac{\partial^2 S_{\text{cry}}}{\partial \Theta\, \partial E_{\text{s}}}\, \dot{E}_{\text{s}} + \Theta\, \frac{\partial S_{\text{cry}}}{\partial \Theta}\, \frac{\dot{E}_{\text{s}}}{\partial E_{\text{s}}} \\ & - \frac{\partial c_{\text{cry}}}{\partial E_{\text{s}}}\, \dot{\Theta} \Bigg\}_{\Theta_m} \\ & \left[\begin{array}{ccc} \Delta X_1 + \Delta u_1 & \Delta X_2 + \Delta u_2 & \Delta X_3 + \Delta u_3 \end{array}\right] . \end{aligned} \tag{A.32}$$

The linearization of the weak form of the balance of energy with respect to the nodal temperature values is

$$\begin{aligned}\left.\frac{\partial G_t^e}{\partial \boldsymbol{\Theta}}\right|_p \Delta \boldsymbol{\Theta}^e = & \int_{(s)} \left(\Delta w_{\text{cry}} - \Delta c_{\text{cry}}\, \dot{\Theta} - c_{\text{cry}}\, \Delta \dot{\Theta}\right) \delta\Theta\, A\, \mathrm{d}s \\ & + \int_{(s)} \Delta Q\, \nabla_{\mathbf{X}}\left(\delta\Theta\right) A\, \mathrm{d}s\,. \end{aligned} \tag{A.33}$$

Subsequently, each part of the integral is evaluated. Partial derivation with respect to temperature and integration yields

$$\begin{aligned}\int_{(s)} \Delta w_{\text{cry}}\, \delta\Theta\, A\, \mathrm{d}s = & \int_{(s)} \delta\Theta\, \frac{\partial w_{\text{cry}}}{\partial \Theta}\, \Delta\Theta\, A\, \mathrm{d}s \\ & = \left[\begin{array}{cc} \delta\Theta_1 & \delta\Theta_2 \end{array}\right] B_3 \left[\begin{array}{cc} 1 & 1 \\ 1 & 1 \end{array}\right] \left[\begin{array}{c} \Delta\Theta_1 \\ \Delta\Theta_2 \end{array}\right] \end{aligned} \tag{A.34}$$

with

$$\begin{aligned} B_3 = \frac{A\,L}{4}\Bigg\{ & -\left(\frac{\partial^2 \Psi_{\text{cry}}}{\partial \Phi\, \partial \Theta} - \frac{\partial^2 \Psi_{\text{cry}}}{\partial \Theta\, \partial \Phi} - \Theta\, \frac{\partial^3\, \Psi_{\text{cry}}}{(\partial \Theta)^2\, \partial \Phi}\right) \dot{\Phi} \\ & - \left(\frac{\partial \Psi_{\text{cry}}}{\partial \Phi} - \Theta\, \frac{\partial^2 \Psi_{\text{cry}}}{\partial \Theta\, \partial \Phi}\right) \frac{\partial \dot{\Phi}}{\partial \Theta} \\ & + \frac{\partial S_{\text{cry}}}{\partial \Theta}\, \dot{E}_{\text{s}} + \Theta\, \frac{\partial^2 S_{\text{cry}}}{(\partial \Theta)^2}\, \dot{E}_{\text{s}} \Bigg\}_{\Theta_m} . \end{aligned} \tag{A.35}$$

ACCEPTED MANUSCRIPT

The heat capacity part reads

$$
\begin{aligned}
&-\int_{(s)} \left(\Delta c_{\text{cry}}\,\dot{\Theta} + c_{\text{cry}}\,\Delta\dot{\Theta}\right)\delta\Theta\,A\,\mathrm{d}s = \\
&-\int_{(s)} \left(\dot{\Theta}\,\frac{\partial c_{\text{cry}}}{\partial\Theta}\,\Delta\Theta + c_{\text{cry}}\,\Delta\dot{\Theta}\right)\delta\Theta\,A\,\mathrm{d}s = \\
&\left[\begin{array}{cc}\delta\Theta_1 & \delta\Theta_2\end{array}\right]\left(-\frac{A\,L\left\{\dot{\Theta}\,\frac{\partial c_{\text{cry}}}{\partial\Theta}\right\}_{\Theta_m}}{4} - \frac{A\,c_{\text{cry}}\,L}{4\,\Delta t}\right)\left[\begin{array}{cc}1 & 1\\ 1 & 1\end{array}\right]\left[\begin{array}{c}\Delta\Theta_1\\ \Delta\Theta_2\end{array}\right],
\end{aligned}
\tag{A.36}
$$

where the time discretization of the temperature is used in the form

$$
\dot{\Theta} = \frac{\Theta^{t_{n+1}} - \Theta^{t_n}}{\Delta t}\,. \tag{A.37}
$$

For the contribution to the residuum,

$$
-\int_{(s)} c_{\text{cry}}\,\dot{\Theta}\,\delta\Theta\,A\,\mathrm{d}s = \left[\begin{array}{cc}\delta\Theta_1 & \delta\Theta_2\end{array}\right]\left(-\frac{A\,c_{\text{cry}}\,L}{2\,\Delta t}\right)\left(\left[\begin{array}{c}1\\1\end{array}\right]\Theta_m - \left[\begin{array}{c}1\\1\end{array}\right]\Theta_m^{t_n}\right) \tag{A.38}
$$

holds. The heat conduction part becomes

$$
\int_{(s)} \Delta Q\,\nabla_{\mathbf{X}}\left(\delta\Theta\right)A\,\mathrm{d}s = \left[\begin{array}{cc}\delta\Theta_1 & \delta\Theta_2\end{array}\right]\left(-\frac{A\,k_{\text{cry}}}{\lambda_{\text{s}}^2\,L}\right)\left[\begin{array}{cc}1 & -1\\ -1 & 1\end{array}\right]\left[\begin{array}{c}\Delta\Theta_1\\ \Delta\Theta_2\end{array}\right]. \tag{A.39}
$$

Finally, the residuum on the right side of the equation can be summarized to

$$
\begin{aligned}
\mathbf{r}_2 = &-\frac{A\,c_{\text{cry}}\,L}{2\,\Delta t}\left[\begin{array}{c}\Theta_m^{t_n}\\ \Theta_m^{t_n}\end{array}\right] + \frac{A\,c_{\text{cry}}\,L}{2\,\Delta t}\left[\begin{array}{c}\Theta_m\\ \Theta_m\end{array}\right] + \frac{k_{\text{cry}}\,A}{\lambda_{\text{s}}^2\,L}\left[\begin{array}{c}\Theta_1 - \Theta_2\\ -\Theta_1 + \Theta_2\end{array}\right] \\
&-\frac{A\,L}{2}\left\{-\left(\frac{\partial\Psi_{\text{cry}}}{\partial\Phi} - \Theta\,\frac{\partial^2\Psi_{\text{cry}}}{\partial\Theta\,\partial\Phi}\right)\dot{\Phi} + \Theta\,\frac{\partial S_{\text{cry}}}{\partial\Theta}\,\dot{E}_{\text{s}}\right\}_{\Theta_m}\left[\begin{array}{c}1\\1\end{array}\right].
\end{aligned}
\tag{A.40}
$$

ACCEPTED MANUSCRIPT

ACCEPTED MANUSCRIPT

The tangent term of Eq. (A.33) can be summarized as

$$\left.\frac{\partial G_t^e}{\partial \boldsymbol{\Theta}}\right|_p = \left[\begin{array}{cc} \delta\Theta_1 & \delta\Theta_2 \end{array}\right] \left[\begin{array}{cc} -B_1 - B_2 + B_3 & B_1 - B_2 + B_3 \\ B_1 - B_2 + B_3 & -B_1 - B_2 + B_3 \end{array}\right] \tag{A.41}$$

with the components

$$B_1 = \frac{k_{\text{cry}}\, A}{\lambda_{\text{s}}^2\, L}\,, \tag{A.42}$$

$$B_2 = \frac{A\, L \left\{\dot{\Theta}\, \frac{\partial c_{\text{cry}}}{\partial \Theta}\right\}_{\Theta_m}}{4} + \frac{A\, c_{\text{cry}}\, L}{4\, \Delta t} \tag{A.43}$$

and B_3 defined in Eq. (A.35).

References

[1] R. Dargazany, V. Khiêm, E. Poshtan, M. Itskov, Constitutive modeling of strain-induced crystallization in filled rubbers, Physical Review E 89 (2014) 022604.

[2] W. Zhou, X. Li, J. Lu, N. Huang, L. Chen, Z. Qi, L. Li, H. Liang, Toughening mystery of natural rubber deciphered by double network incorporating hierarchical structures, Scientific Reports 4 (2014) 7502.

[3] G. Mitchell, A wide-angle X-ray study of the development of molecular orientation in crosslinked natural rubber, Polymer 25 (1984) 1562–1572.

[4] M. Tosaka, A route for the thermodynamic description of strain-induced crystallization in sulfur-cured natural rubber, Macromolecules 42 (2009) 6166–6174.

[5] M. Leitner, Young's modulus of crystalline, unstretched rubber, Transactions of the Faraday Society 51 (1955) 1015–1021.

[6] A. Gent, S. Kawahara, J. Zhao, Crystallization and strength of natural rubber and synthetic cis-1,4-polyisoprene, Rubber Chemistry and Technology 71 (1998) 668–678.

[7] W. Mars, A. Fatemi, A literature survey on fatigue analysis approaches for rubber, International Journal of Fatigue 24 (2002) 949–961.

[8] R. Dargazany, M. Itskov, A network evolution model for the anisotropic Mullins effect in carbon black filled rubbers, International Journal of Solids and Structures 46 (2009) 2967–2977.

ACCEPTED MANUSCRIPT

ACCEPTED MANUSCRIPT

[9] L. Treloar, The Physics of Rubber Elasticity, Clarendon Press, Oxford, 1975.

[10] L. Wood, N. Bekkedahl, Crystallization of unvulcanized rubber at different temperatures, Journal of Applied Physics 17 (1946) 362.

[11] A. Phillips, A. Bhatia, P. Zhu, G. Edward, Shish formation and relaxation in sheared isotactic polypropylene containing nucleating particles, Macromolecules 44 (2011) 3517–3528.

[12] M. Tosaka, Strain-induced crystallization of crosslinked natural rubber as revealed by X-ray diffraction using synchrotron radiation, Polymer Journal 39 (2007) 1207–1220.

[13] K. Brüning, K. Schneider, S. Roth, G. Heinrich, Kinetics of strain-induced crystallization in natural rubber studied by WAXD: Dynamic and impact tensile experiments, Macromolecules 45 (2012) 7914–7919.

[14] N. Candau, L. Chazeau, J.-M. Chenal, C. Gauthier, J. Ferreira, E. Munch, C. Rochas, Characteristic time of strain induced crystallization of crosslinked natural rubber, Polymer 53 (2012) 2540–2543.

[15] G. Yeh, K. Hong, Strain-induced crystallization. Part III: Theory, Polymer Engineering and Science 19 (1979) 395–400.

[16] P. Flory, Thermodynamics of crystallization in high polymers. I. Crystallization induced by stretching, The Journal of Chemical Physics 15 (1947) 397–408.

[17] M. Kroon, A constitutive model for strain-crystallising rubber-like materials, Mechanics of Materials 42 (2010) 873–885.

[18] M. Negahban, Modeling the thermomechanical effects of crystallization in natural rubber: I. The theoretical structure, International Journal of Solids and Structures 37 (2000) 2777–2789.

[19] M. Negahban, Modeling the thermomechanical effects of crystallization in natural rubber: II. Elementary thermodynamic properties, International Journal of Solids and Structures 27 (2000) 2791–2809.

[20] M. Negahban, Modeling the thermomechanical effects of crystallization in natural rubber: III. Mechanical properties, International Journal of Solids and Structures 37 (2000) 2811–2824.

[21] R. Laghmach, T. Biben, L. Chazeau, J. Chenal, E. Munch, C. Gauthier, Strain-induced crystallization in natural rubber: A model for the microstructural evolution, in: N. Gil-Negrete, A. Alonso (Eds.), Constitutive Models for Rubber VIII, CRC Press, Taylor &

ACCEPTED MANUSCRIPT

Francis Group, London, 2013, pp. 473–477.

[22] R. Laghmach, N. Candau, L. Chazeau, E. Munch, T. Biben, Phase field modelling of strain induced crystal growth in an elastic matrix, The Journal of Chemical Physics 142 142 (2015) 244905.

[23] S. Poompradub, M. Tosaka, S. Kohjiya, Y. Ikeda, S. Toki, I. Sics, B. Hsiao, Mechanism of strain-induced crystallization in filled and unfilled natural rubber vulcanizates, Journal of Applied Physics 97 (2005) 103529.

[24] S. Toki, I. Sics, S. Ran, L. Liu, B. Hsiao, Molecular orientation and structural development in vulcanized polyisoprene rubbers during uniaxial deformation by in situ synchrotron X-ray diffraction, Polymer 44 (2003) 6003–6011.

[25] J. Guilie, L. Thien-Nga, P. Le Tallec, Micro-sphere model for strain-induced crystallisation and three-dimensional applications, Journal of the Mechanics and Physics of Solids 81 (2015) 58–74.

[26] R. Rastak, C. Linder, A non-affine micro-macro approach to strain-crystallizing rubber-like materials, Journal of the Mechanics and Physics of Solids 111 (2018) 67–99.

[27] V. Khiêm, M. Itskov, A micromechanical model for dynamic strain-induced crystallization in filled natural rubbers, in: B. Marvalova, I. Petrikova (Eds.), Constitutive Models for Rubber IX, CRC Press, Taylor & Francis Group, London, 2015, pp. 521–527.

[28] K. Loos, M. Johlitz, A. Lion, L. Palgen, J. Calipel, New ideas to represent strain induced crystallization in elastomers, in: A. Lion, M. Johlitz (Eds.), Constitutive Models for Rubber X, CRC Press, Taylor & Francis Group, London, 2017, pp. 199–205.

[29] S. Mistry, S. Govindjee, A micro-mechanically based continuum model for strain-induced crystallization in natural rubber, International Journal of Solids and Structures 51 (2014) 530–539.

[30] N. Nateghi, M. Keip, C. Miehe, An affine full network model for strain-induced crystallization in rubbers, in: A. Lion, M. Johlitz (Eds.), Constitutive Models for Rubber X, CRC Press, Taylor & Francis Group, London, 2017, pp. 121–127.

[31] K. Schneider, L. Zybell, J. Domurath, G. Heinrich, S. Roth, A. Rothkirch, W. Ohm, Investigation of time dependence of dissipation and strain induced crystallization in natural rubber under cyclic and impact loading, in: A. Lion, M. Johlitz (Eds.), Constitutive Models for Rubber X, CRC Press, Taylor & Francis Group, London, 2017, pp. 173–177.

ACCEPTED MANUSCRIPT

[32] J. Plagge, T. Spratte, M. Wunde, M. Klüppel, Thermo-mechanical properties of strain-crystallizing elastomer nanocomposites, in: A. Lion, M. Johlitz (Eds.), Constitutive Models for Rubber X, CRC Press, Taylor & Francis Group, London, 2017, pp. 489–494.

[33] M. Kaliske, R. Behnke, Material laws of rubbers, in: S. Kobayashi, K. Müllen (Eds.), Encyclopedia of Polymeric Nanomaterials, Springer-Verlag, Berlin, 2015, pp. 1187–1197.

[34] S. Reese, S. Govindjee, Theoretical and numerical aspects in the thermo-viscoelastic material behaviour of rubber-like polymers, Mechanics of Time-Dependent Materials 1 (1998) 357–396.

[35] M. Kaliske, G. Heinrich, An extended tube-model for rubber elasticity: Statistical-mechanical theory and finite element implementation, Rubber Chemistry and Technology 72 (1999) 602–632.

[36] R. Behnke, M. Kaliske, The extended non-affine tube model for crosslinked polymer networks: Physical basics, implementation, and application to thermomechanical finite element analyses, in: K. Stöckelhuber, A. Das, M. Klüppel (Eds.), Designing of Elastomer Nanocomposites: From Theory to Applications, Vol. 275 of Advances in Polymer Science, Springer-Verlag, Berlin, 2016, pp. 1–70.

[37] C. Miehe, Entropic thermoelasticity at finite strains. Aspects of the formulation and numerical implementation, Computer Methods in Applied Mechanics and Engineering 120 (1995) 243–269.

[38] K. Brüning, K. Schneider, S. Roth, G. Heinrich, Kinetics of strain-induced crystallization in natural rubber: A diffusion-controlled rate law, Polymer 72 (2015) 52–58.

[39] J. Marchal, Cristallisation des caoutchoucs chargés et non chargés sous contrainte: Effet sur les chaînes amorphes, Ph.D. thesis, UFR Scientifique D'Orsay École Doctorale, Université Paris Sud – Paris XI (2006).

[40] R. Behnke, Thermo-mechanical modeling and durability analysis of elastomer components under dynamic loading, Ph.D. thesis, Fakultät Bauingenieurwesen, Technische Universität Dresden (2015).

[41] G. Meschke, P. Helnwein, Large-strain 3D-analysis of fibre-reinforced composites using rebar elements: Hyperelastic formulations for cords, Computational Mechanics 13 (1994) 241–254.

[42] R. Behnke, M. Kaliske, Thermo-mechanically coupled investigation of steady state rolling

ACCEPTED MANUSCRIPT

tires by numerical simulation and experiment, International Journal of Non-Linear Mechanics 68 (2015) 101–131.

[43] J.-B. Le Cam, J. Samaca Martinez, X. Balandraud, E. Toussaint, J. Caillard, Thermomechanical analysis of the singular behavior of rubber: Entropic elasticity, reinforcement by fillers, strain-induced crystallization and the Mullins effect, Experimental Mechanics 55 (2015) 771–782.

[44] J.-B. Le Cam, Energy storage due to strain-induced crystallization in natural rubber: The physical origin of the mechanical hysteresis, Polymer 127 (2017) 166–173.

[45] P. de Gennes, Kinetics of diffusion-controlled processes in dense polymer systems: I. Nonentangled regimes, The Journal of Chemical Physics 76, 76 (1982) 3316–3321.

[46] R. Behnke, M. Kaliske, Finite-element-based analysis of reinforcing cords in rolling tires: Influence of mechanical and thermal cord properties on tire response, Tire Science and Technology submitted.

[47] R. Behnke, M. Mundil, C. Birk, M. Kaliske, A physically and geometrically nonlinear scaled-boundary-based finite element formulation for fracture in elastomers, International Journal for Numerical Methods in Engineering 99 (2014) 966–999.

[48] C. Miehe, Computational micro-to-macro transitions for discretized microstructures of heterogeneous materials at finite strains based on the minimization of averaged incremental energy, Computer Methods in Applied Mechanics and Engineering 192 (2003) 559–591.

[49] C. Miehe, S. Göktepe, F. Lulei, A micro-macro approach to rubber-like materials. Part I: The non-affine micro-sphere model of rubber elasticity, Journal of the Mechanics and Physics of Solids 52 (2004) 2617–2660.

[50] C. Miehe, S. Göktepe, A micro-macro approach to rubber-like materials. Part II: The micro-sphere model of finite rubber viscoelasticity, Journal of the Mechanics and Physics of Solids 53 (2005) 2231–2258.

[51] R. Fleischhauer, M. Božić, M. Kaliske, A novel approach to computational homogenization and its application to fully coupled two-scale thermomechanics, Computational Mechanics 58 (2016) 769–796.

[52] N. Candau, R. Laghmach, L. Chazeau, J.-M. Chenal, C. Gauthier, T. Biben, E. Munch, Temperature dependence of strain-induced crystallization in natural rubber: On the presence of different crystallite populations, Polymer 60 (2015) 115–124.

ACCEPTED MANUSCRIPT

ACCEPTED MANUSCRIPT

[53] N. Candau, R. Laghmach, L. Chazeau, J.-M. Chenal, C. Gauthier, T. Biben, E. Munch, Influence of strain rate and temperature on the onset of strain induced crystallization in natural rubber, European Polymer Journal 64 (2015) 244–252.

[54] M. Freund, J. Ihlemann, Generalization of one-dimensional material models for the finite element method, Journal of Applied Mathematics and Mechanics 90 (2010) 399–417.

[55] M. Freund, H. Lorenz, D. Juhre, J. Ihlemann, M. Klüppel, Finite element implementation of a microstructure-based model for filled elastomers, International Journal of Plasticity 27 (2011) 902–919.

[56] A. Lion, M. Johlitz, A thermodynamic approach to model the caloric properties of semicrystalline polymers, Continuum Mechanics and Thermodynamics 28 (2016) 799–819.

ACCEPTED MANUSCRIPT